Supplementary Information for

"1,2,3-Triazole-Derived Pincer-Type Mesoionic Carbene Complex of Iron(II): Carbonyl Elimination, Hydrosilylation of Aromatic Aldehydes via Concerted Reaction with Hydrosilane and Base"

Kouki Matsubara,* Yuji Yamada, Haruka Iwasaki, Hayao Ikeda, Yuki Kanetsugu, Satoshi Kawata and Yuji Koga

Department of Chemistry, Fukuoka University, 8-19-1 Nanakuma, Fukuoka 814-0180, JAPAN

Contents

S-1. Characterization of Iron Complexes

S-1-1. Complex 2-BPh_4

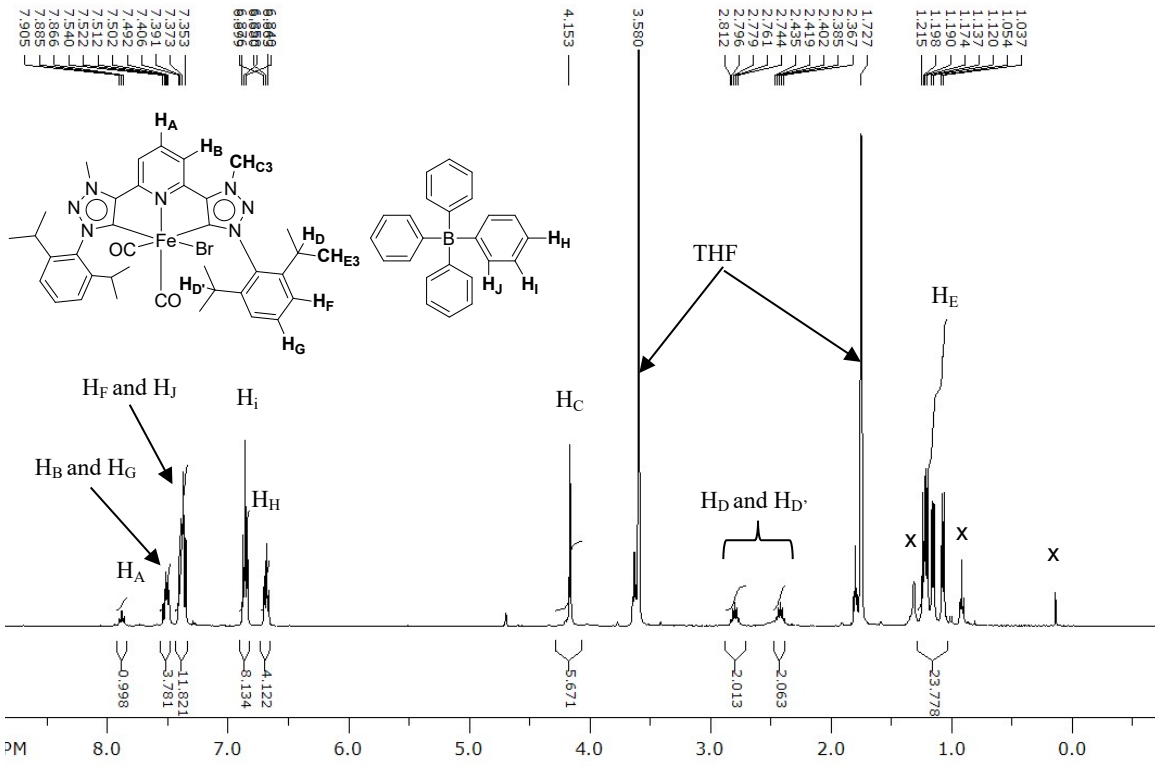

Figure S1. ^{1}H NMR (400 MHz) spectrum of **2-BPh_4** in THF-d_8

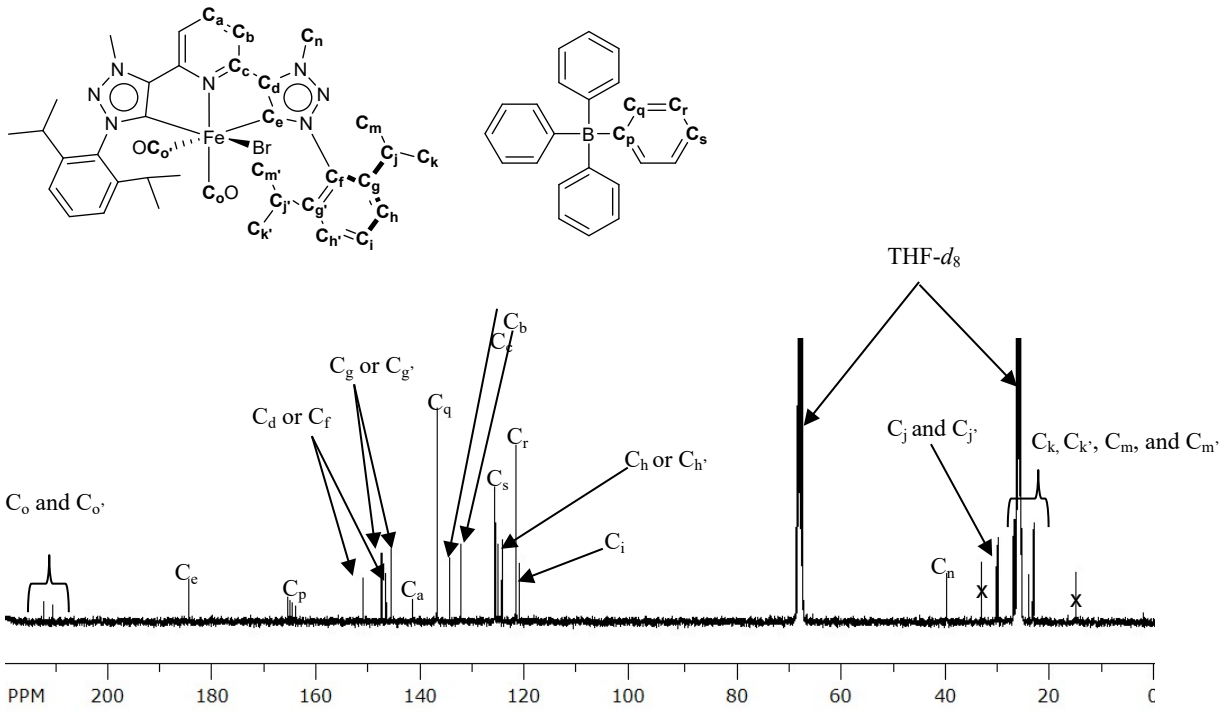

Figure S2. ^{13}C NMR (100 MHz) spectrum of **2-BPh_4** in THF-d_8

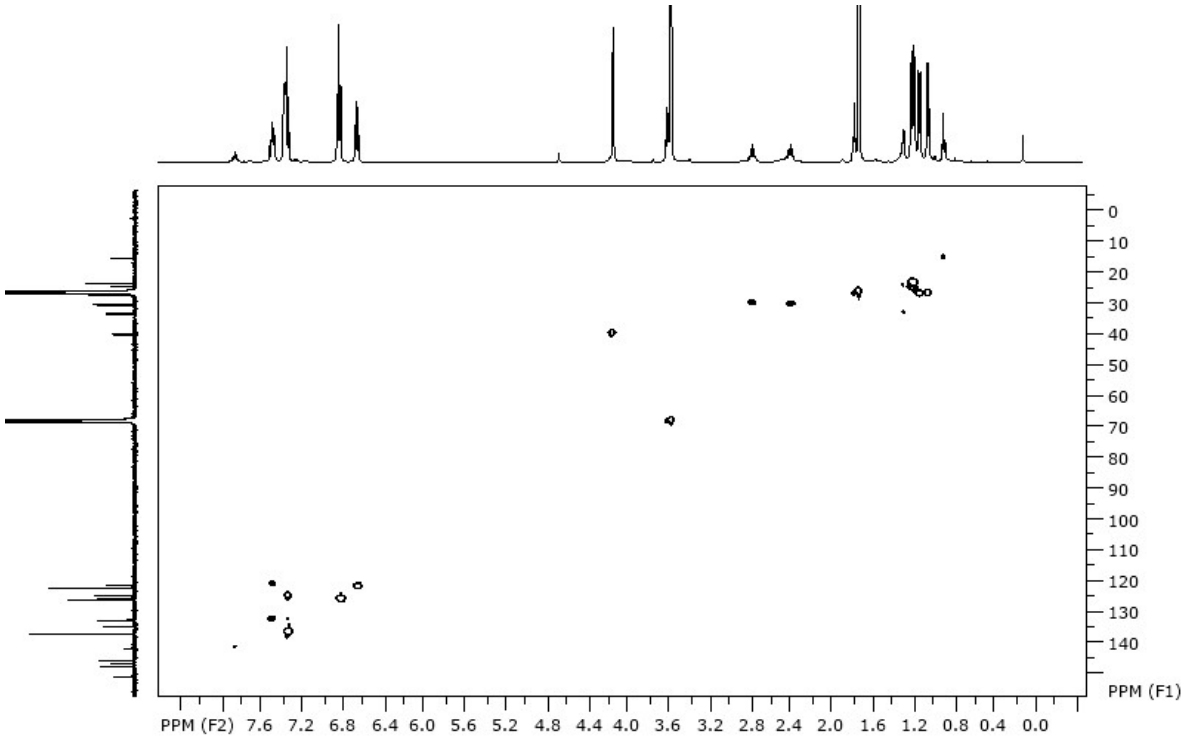

Figure S3. $^{1}H/^{13}C$ HSQC spectrum of **2-BPh$_4$** (THF-d_8; 25 °C)

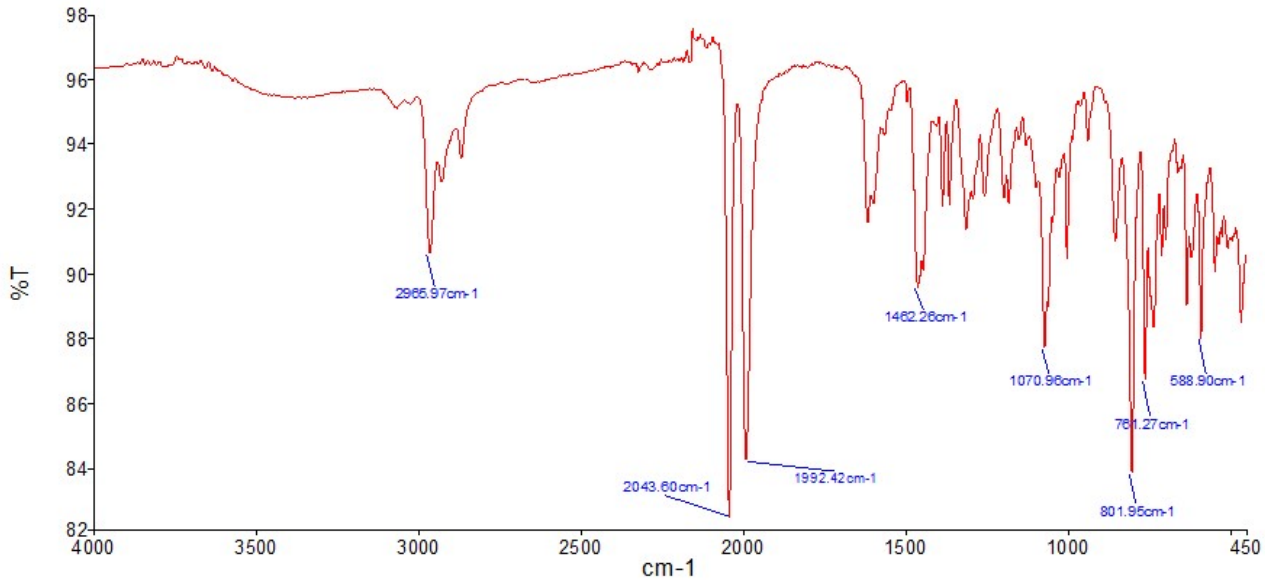

Figure S4. IR spectrum of **2-BPh$_4$** (solid state)

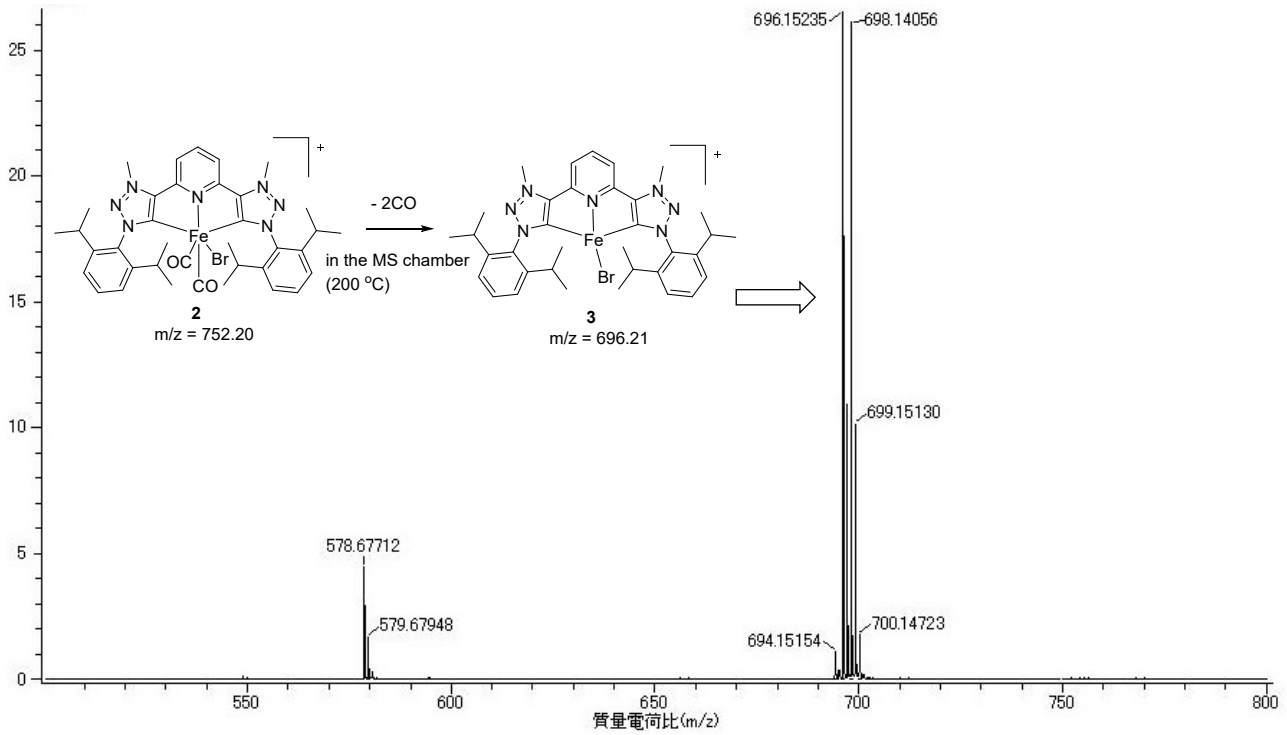

Figure S5. ESI-TOF MS(+) spectrum for **2-BPh$_4$** in CH_3CN. Peaks due to the CO-elimination product (m/z = 696.15, calcd. for 696.21) were observed, while mono-CO and bis-CO complexes (m/z = 724.21 and 752.20, respectively) were not detected from **2-BPh$_4$**.

S-1-2. Complex 2

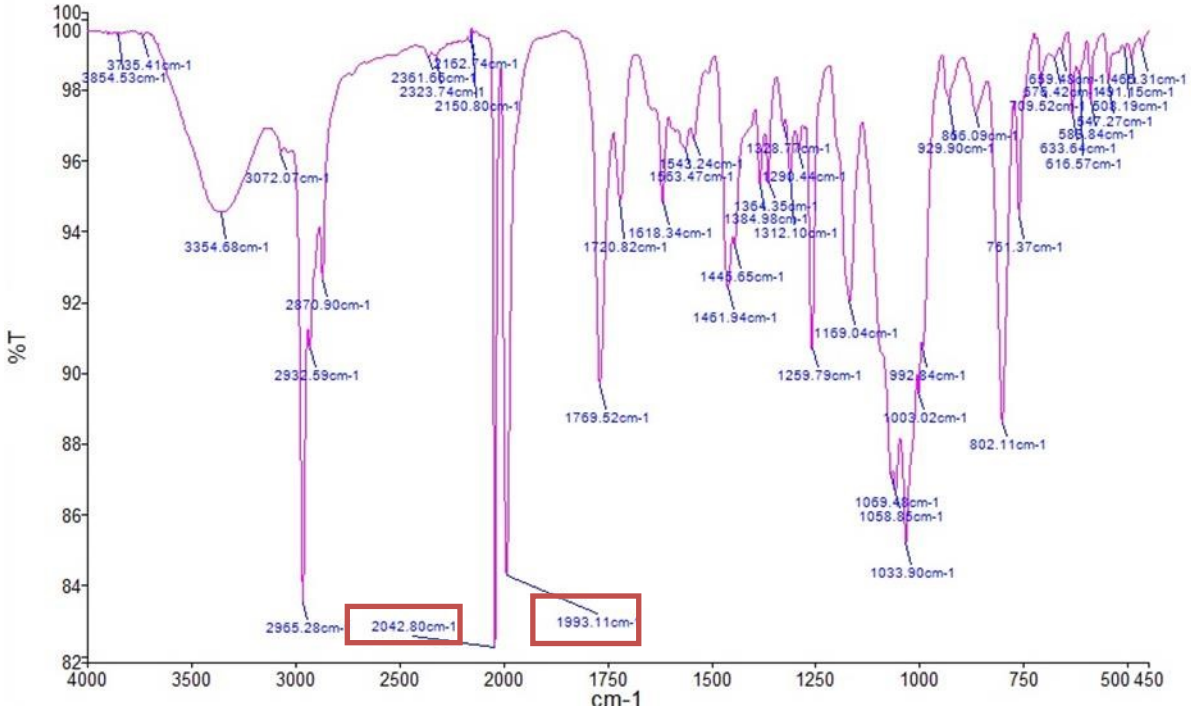

Figure S6. IR spectrum of **2** (solid state), before anion exchange with $NaBPh_4$.

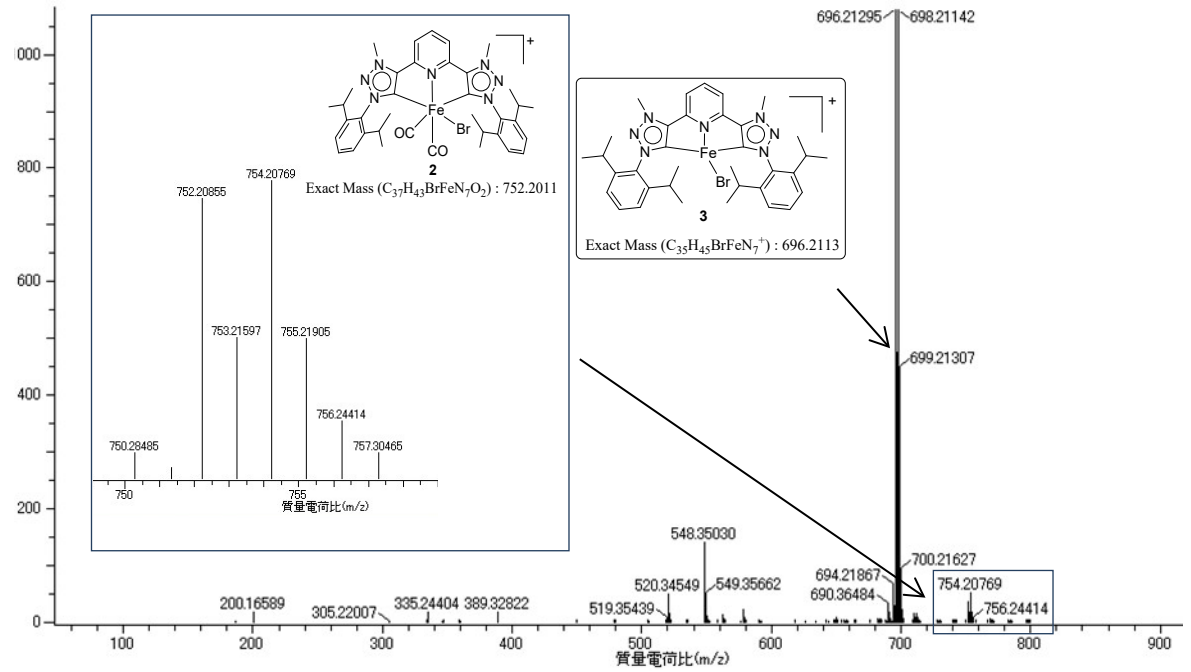

Figure S7. ESI-TOF MS(+) spectrum for **2** in CH_3CN. Peaks due to the cationic part of the bis-CO complex **2** (m/z = 752.20, calcd. for 752.20) were detected, whereas peaks can be mainly observed from the CO-elimination product **3** (m/z = 696.15, calcd. for 696.21).

S-2. Formation of 3 and Characterization with ESI-TOF MS and ^{57}Fe Mössbauer Analysis

Synthetic procedure to yield complex 3

To a glass bottle were charged $FeBr_2$ (29.1 mg 0.136 mmol), $NaBPh_4$ (46.4 mg, 0.136 mmol) and THF (3.2 mL) and stirred over night at room temperature. To another glass bottle were charged NaO^tBu (29.6 mg, 0.308 mmol), ether (0.8 mL) and **1** (100 mg, 0.136 mmol), and the mixture was stirred for 1 h and then filtered through celite with additional portion of ether (2.0 mL) and added to the mixture containing iron. The resulting mixture was stirred for 5 h at room temperature. After the mixture was filtered through celite, the resulting solution was removed under reduced pressure. The crude product was precipitated over the THF solution with addition of excess ether (0.139 mg, 11%). After removal of the supernatant, recrystallization over pyridine/hexane at -30°C gave orange prismatic crystals. ESI-TOF MS, found: 696.26 (m/z), calcd for $C_{35}H_{43}N_7Fe_1Br_1$: 696.21 (m/z).

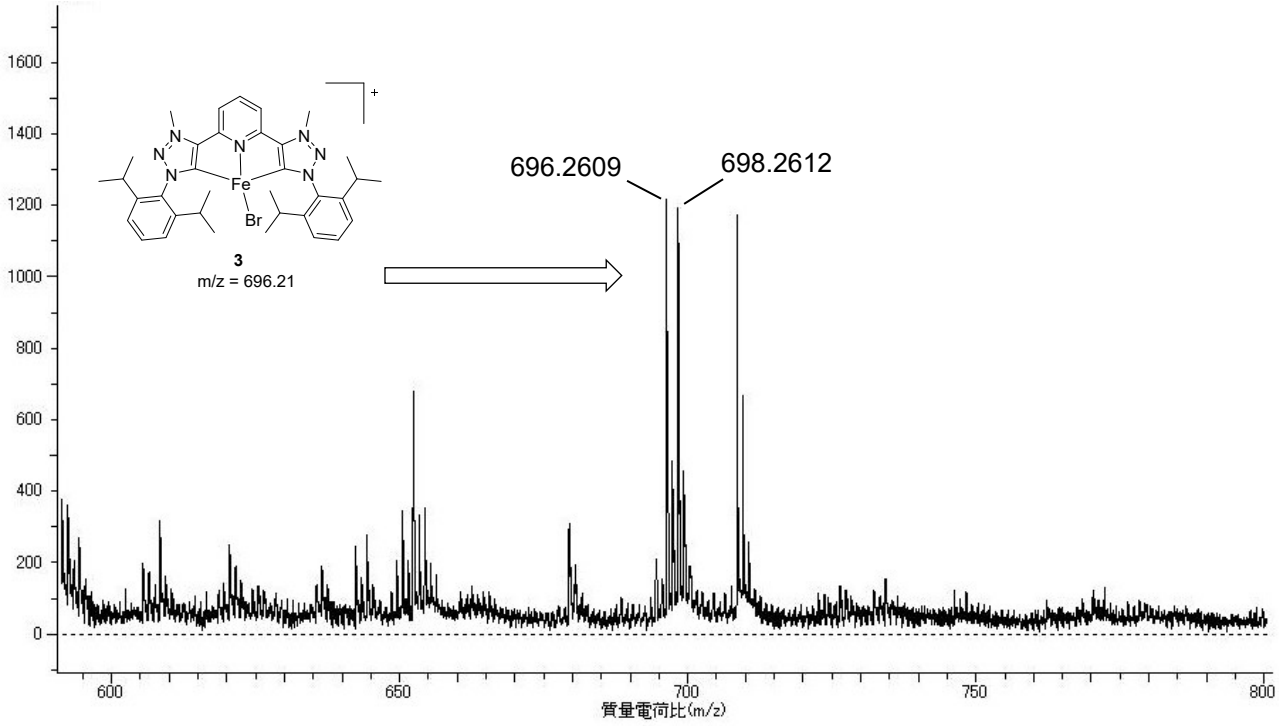

Figure S8. ESI-TOF MS(+) spectrum for **3** in CH_3CN, which was synthesized from **1** and $FeBr_2(thf)_{1.5}$ in ether/THF, where $FeBr_2(thf)_{1.5}$ was previously treated with $NaBPh_4$. Most of the compound probably decomposed by small amount of contaminated water and/or air before the measurement in the acetonitrile solution and small amount of **5a** was detected as peaks around 696.26 (m/z) (calcd. for $C_{35}H_{43}N_7Fe_1Br_1$: 696.21 (m/z)).

S-3. Study on CO Elimination Process

Because clear evidence of CO loss from **2-BPh$_4$** could not be obtained using TG/DTA, we performed IR spectroscopic and ESI-MS analyses of the sample dissolved in THF in an inert gas atmosphere just after the TG/DTA measurements up to 180 ºC, followed by rapid cooling to room temperature. Although it was difficult to conclude that the weight loss corresponded exactly to loss of the carbonyl ligands, the absorbance attributed to carbonyl ligands at around 2000 cm^{-1} in the IR spectrum disappeared, and the mass ion peak at *m*/*z* 696.32, assignable to $[Fe(MIC)Br]^+$, was observed (see the Supporting Information). The IR spectrum of the decomposed product was similar to that of **3** prepared using the method shown in Scheme 2. These results suggest that the dicarbonyl complex thermally decomposes at least up to 180 ºC, accompanied by elimination of the carbonyl ligands.

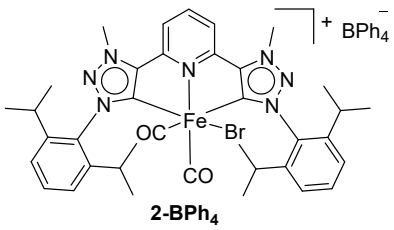

2-BPh$_4$

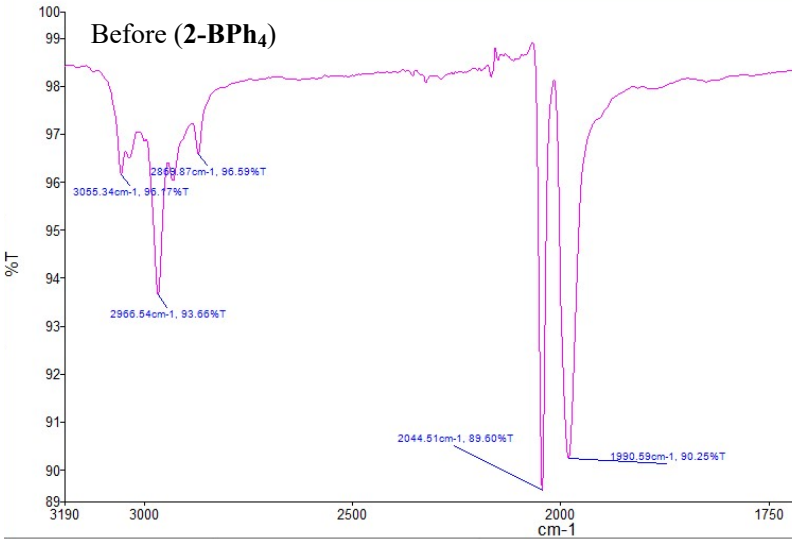

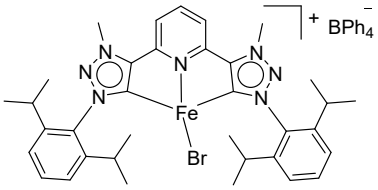

3

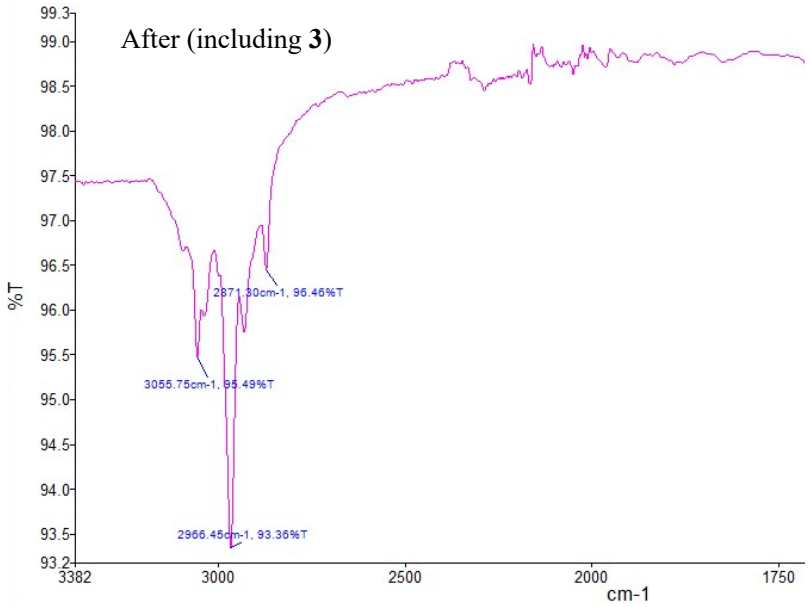

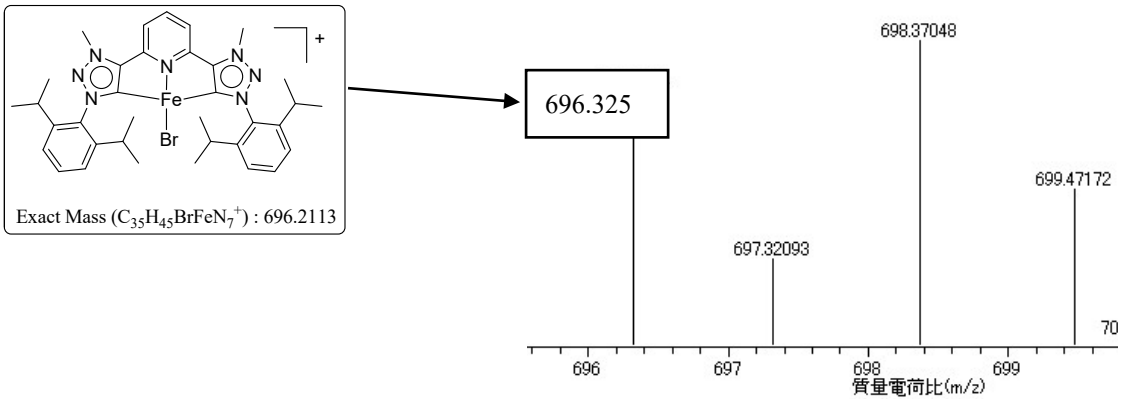

Figure S9. The heating reaction of **2-BPh$_4$** was monitored with IR and ESI- MS spectroscopies in the solid states and in the THF solution. After the reaction, there were no CO stretching bands and mass ion peaks from **2**, but the ion peak from **3** can be detected.

S-4. DFT Calculations

S-4-1. Computational details of CO abstraction

All the calculations were performed using the GAUSSIAN 09 packages.[2] The geometry optimization was performed using the density functional theory (DFT) with the B3LYP functional[3] without symmetry restriction. Furthermore, the nature of stationary points, that is local minimum or saddle point, was checked by the vibrational frequency analysis at the same level. This functional has been extensively used in the theoretical studies on the "spin-forbidden" reaction mechanism of similar Fe complexes because of its relatively good reproducibility to the reaction energy of complex formation.[4] The relativistic effective core potential (ECP) and basis set of Los Alamos ECP plus DZ (LANL2DZ)[5] was applied to the iron atom, and a standard 6-31G(d) basis set was employed for all other atoms.

Reaction paths including geometry optimization of transition states within the same spin state were calculated using the synchronous transit-guided quasi-Newton method.[6] Minimum potential energy surfaces (PESs) toward the dissociation reaction of CO ligand were obtained as a function of Fe−CO bond length by optimizing geometrical parameters except for the fixed Fe−CO bond length. Next, intersystem crossing points between two adiabatic PESs of the different spin states were searched in simple approximation that the spin-orbit coupling, determining a hopping yield from the initial PES to the objective one, is independent of the complex geometry. In such points, both the geometry and the energy are the identical on two spin states. Therefore, two ways were examined; one was to calculate a PES of the objective spin state against the CO dissociation coordinate at the same geometries which had been obtained by the geometry optimization for the minimum-energy PES of the initial spin state as mentioned above. If the energy crossing point exists between these two PESs, a change in spin state may occur through it on the way to the dissociation of a CO ligand. Another was to obtain an energy crossing between PESs of both spin states as a function of the geometry optimization steps starting from the unstable geometry which was local minimum in the other spin state. The maximum size for an optimization step was set to 0.01 Bohr or radians in order to obtain fine steps. Although the reaction PESs reported in this article do not involve zero-point energy (ZPE), the free energy values of stable reaction intermediates and products are obtained at 298.15 K and 1 atm with ZPE and thermal energy corrections based on the vibrational frequency calculation.

As for transmetallation with hydrosilane, where the dispersion interaction between bulky substituents is not negligible for the stability of the complex, in order to improve the accuracy of reaction energy, the dispersion correction and the bulk solvent effect were included by the single point calculation using the dispersion-corrected B3LYP functional with Becke–Johnson damping (B3LYP-D3BJ)[7] and polarizable continuum model (PCM[8] for toluene solvent ($\varepsilon = 2.3741$) using the same ECP and basis sets at the optimized vacuum-geometries. This calculation level was denoted by PCM(toluene)-B3LYP-D3BJ//B3LYP/ECP(LanL2DZ) for Fe and 6-31G(d) for others. All the computation was carried out using the computer facilities at Research Institute for Information Technology, Kyushu University.

S-4-2. Calculated Details of CO-Elimination Mechanism

The loss of CO ligands from $[Fe(MIC)Br(CO)_2]^+$ (**2**) was examined by means of DFT calculation with B3LYP functional (see Computational details). Figure S10 shows the energy profiles of reactants and CO-dissociation products in the different spin states with S = 0-2, which corresponds to singlet, triplet, and quintet, respectively. As for mono-CO dissociated complex, two stable isomers are obtained in the singlet and quintet states.

One has the *apical*-coordination of CO toward Br, and the other is *equatorial* one. The latter is the global minimum in the singlet state, but its stability is opposite in the quintet one. The geometry optimization of doubly CO-dissociated products provides single structure in each spin state, where the complex planarity depends on the spin states as indicated by the N−Fe−Br angle in the figure. From the calculated relative energies, it is found that the singlet state becomes unstable with the first CO dissociation, resulting in a crossing point with the spin-triplet potential energy surface (PES), and that the further dissociation gives rise to the relatively stable quintet state. Evaluating the corresponding free energies (ΔG^{298} = 46.0, 21.6, and 13.8 kcal/mol in order of increasing spin state) of doubly CO-dissociated products also, the final product is easily predicted to be quintet. Thus, it is considered that two intersystem crossing (ISC) reactions probably occur; one is spin-hopping from singlet to triplet state through the first CO dissociation, and the other is the "spin-forbidden" reaction between triplet and quintet states by the second one. Such a change in spin state proceeds via a crossing point of two PESs, where both the energy and geometry are the identical on the two surfaces. In the following section, we will discuss the two crossing points.

First, in order to investigate the first crossing point, the minimum-energy singlet PES and the triplet PES at the same geometry were calculated as a function of the dissociative coordinate of CO ligand which is coordinated at *apical*- or *equatorial*-position with respect to Br. Starting from the singlet reactant denoted by **^{1}A** in the center of Figure S11, the left side indicates the PES toward the dissociation reaction of apical-CO ligand, and the right is the case of equatorial-one. The former shows that there is a crossing point on the way to dissociating, i.e. at the Fe−CO bond length of 2.872 Å, and that the barrier associated with this spin-hopping reaction is 30.7 kcal/mol. After this point, the further elongation gives rise to the stable triplet intermediate of **^{3}A**. The PES for the subsequent ligand dissociation from **^{3}A** to **^{3}B** exhibits significantly gentle uphill due to the Fe-CO distance elongated sufficiently. On the other hand, no crossing point against *equatorial*-CO dissociation means that this reaction proceeds through the spin-singlet minimum-energy dissociation path without transition states and that it forms stable singly CO-dissociation product in the singlet spin state (**^{1}B'**), followed by a spin-hopping accompanied by structural change toward **^{3}B'**, which is geometry-optimized with restriction of the triplet spin state. Comparing both the barrier heights, the former is considered to be slightly favorable. Furthermore, since the calculated transition state between **^{3}B** and **^{3}B'** has the relatively low energy of 32.1 kcal/mol (not shown), it is distinctly possible to occur the isomerization from **^{3}B'** to more stable **^{3}B**.

Next, we investigated not only further dissociation process of **^{3}B** but also a change in spin state from the triplet to quintet state prior to it, because the energies and the geometries of **^{3}B** are resemble to those of the spin-quintet complex as seen in Figure S12. The right side in Figure S12 exhibits PESs in the former reaction process, while the left corresponds to the CO dissociation following ISC from **^{3}B** to **^{5}B**. Note that both the processes provide the same product denoted by **^{5}C**. However, two reactions exhibit the distinct difference in barrier height. The spin-hopping from **^{3}B** to **^{5}B** needs the low energy of only 39.2 kcal/mol in order to exceed the barrier, and the subsequent dissociation toward **^{5}C** has no transition state. Alternatively, the direct dissociation of **^{3}B** may occur. The result that two PESs do not intersect with each other in that case suggests that ISC takes place after forming **^{3}C** by the structural change toward the geometry optimized in quintet spin state. However, due to the low stability of **^{3}C** (+48.8 kcal/mol), the barrier of transition state in this reaction, 53.9 kcal/mol, is much higher than the other path. Thus, it is concluded that the second dissociation reaction progresses after a change in spin state from **^{3}B** to **^{5}B**.

The minimum-energy path for the above-mentioned dissociation of CO ligands from the spin-singlet reactant, **2**, is summarized in Figure S13. Starting from the initial reactant (^{1}**A**), ISC to triplet state occurs at the elongated Fe-CO bond length of 2.872 Å on the way to the first dissociation of CO ligand which is apical-coordinated with respect to Br. After the crossing point is reached, the energy relaxation along the PES downhill results in ^{3}**A** where the Fe-CO bond length is considerably elongated. The PES for the subsequent dissociation from ^{3}**A** to mono-CO dissociation product, ^{3}**B**, exhibits significantly gentle uphill. Furthermore, a slight increase in the N−Fe−Br angle of 12.2° and a significant elongation in the Fe−CO bond distance of 0.247 Å provide the spin-hopping to ^{5}**B**. The barrier height associated with this step relative to ^{3}**B** is estimated to be 10.7 kcal/mol. At the last, a loss of the second CO ligand accompanied by a distinct change in Br position forms the final product (^{5}**C**) without transition states. Although its dissociation energy seems very small (8.9 kcal/mol), it is concluded that the rate-determining step in overall reaction path is this second dissociation, on the basis of lower energies of transition states for ISC.

S-4-3. Optimized Geometries of Local Minima for Transmetallation Reaction with Hydrosilane

The transmetallation reaction path of $[Fe(MIC)Br(CO)_2]^+$ (**2**) with hydrosilane was examined with PCM(toluene)-B3LYP-D3BJ/6-311G(d,p)//B3LYP/ECP(LanL2DZ) for Fe and 6-31G(d) for others. The optimized geometries of local minima and TSs in Figure 7 are shown in Figure S14. Both the proposed initial process of addition of MeOK (**A**) and ligand exchange by silane (**A'**) are shown. The interatomic distance between bromine ligand and potassium ion is similar in **A** and **B**, but their stability by solvation of MeOK is slightly different because of dispersion interaction with bulky silanes; for example, the complex **B** has a sufficiently close distance between the oxygen of MeOK and silane atoms, 4.152 Å. The TS_{BC} structure demonstrates a closer distances to 2.984 Å, suggesting the formation of Si-O bond.

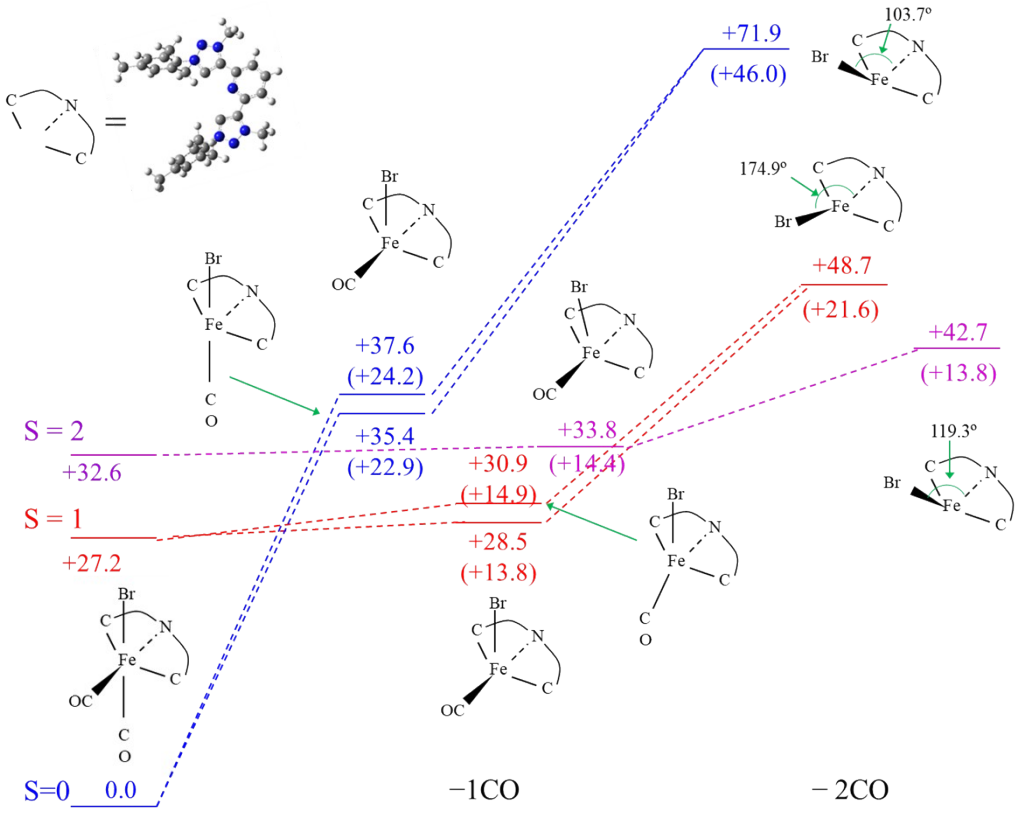

Figure S10. Energy profiles and simplified structures of singlet-$[Fe(MIC)Br(CO)_2]^+$ (2) and ligand-dissociation products in the different spin states of S = 0-2, calculated with B3LYP/ECP(LANL2DZ) for Fe and 6-31G(d) for others. The inserted values indicate the relative electronic energies without zero-point vibrational energy correction in kcal/mol against the most stable spin-singlet reactant. Numbers in parentheses indicate the free energies at 298.15 K and 1atm (ΔG_{298}) associated with the dissociation reaction. Two isomers for singly CO-dissociated complexes were obtained in S = 0 and 1, where CO ligand is located at apical and equatorial position, while that in S = 2 was converged into the same structure within the geometry optimization step. For the doubly CO-dissociated products, the N−Fe−Br angle in each spin state is also shown.

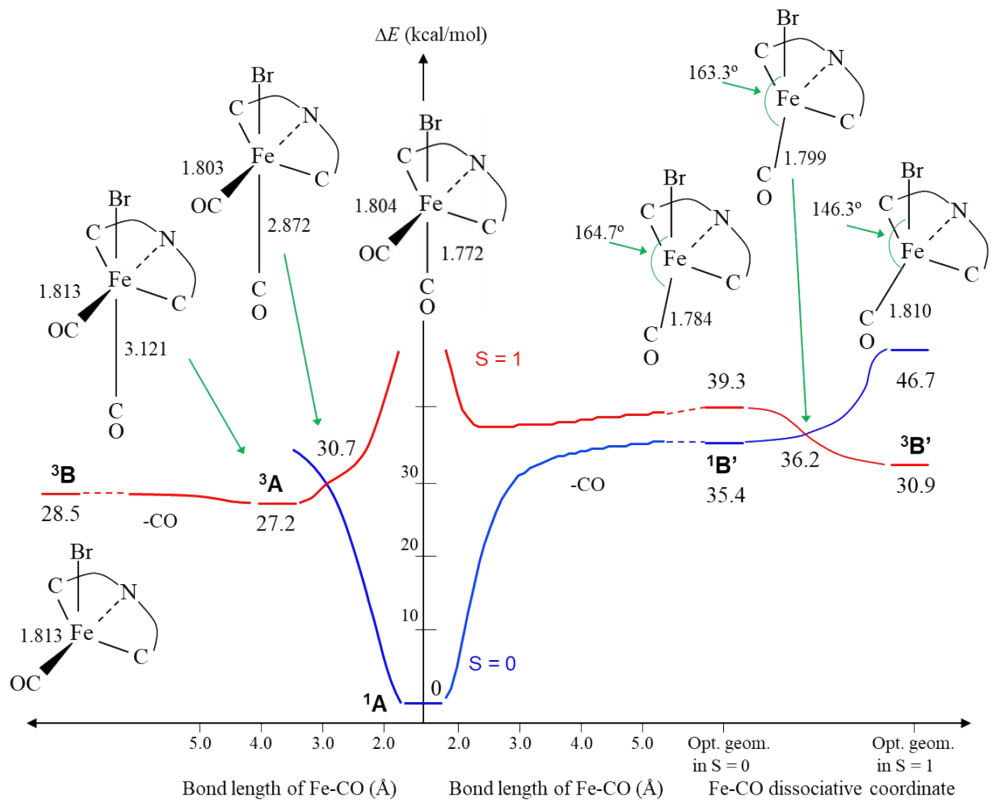

Figure S11. Potential energy curves of spin-singlet and triplet states associated with dissociation reaction of the *apical*-CO ligand with respect to Br from spin-singlet **2** denoted by **^{1}A** (left) and those of *cis*-CO one (right). The inserted values indicate the relative energies in kcal/mol to ^{1}A. Bond lengths of Fe−CO and N−Fe−Br angles in local minimums and transition states are also shown. The broken curves indicate shortened dissociative regions.

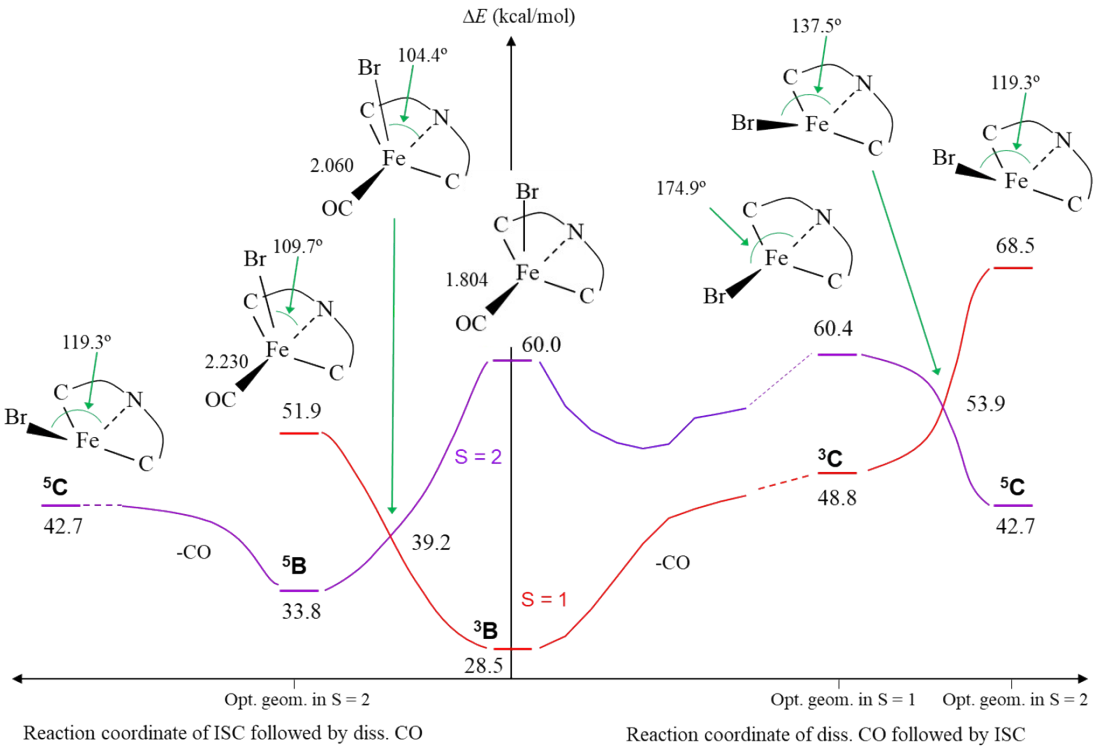

Figure S12. Potential energy curves of spin-triplet and quintet states associated with the CO dissociation following ISC from **^{3}B** to **^{5}B** (left) and further dissociation process of **^{3}B** prior to spin-hopping from triplet to quintet state (right). Both the processes provides the same final product denoted by ^{5}C. The inserted values indicate the relative energies in kcal/mol to **^{1}A** in Figure 4. Bond lengths of Fe−CO and N−Fe−Br angles in local minimums and transition states are also shown. The broken curves indicate shortened dissociative regions.

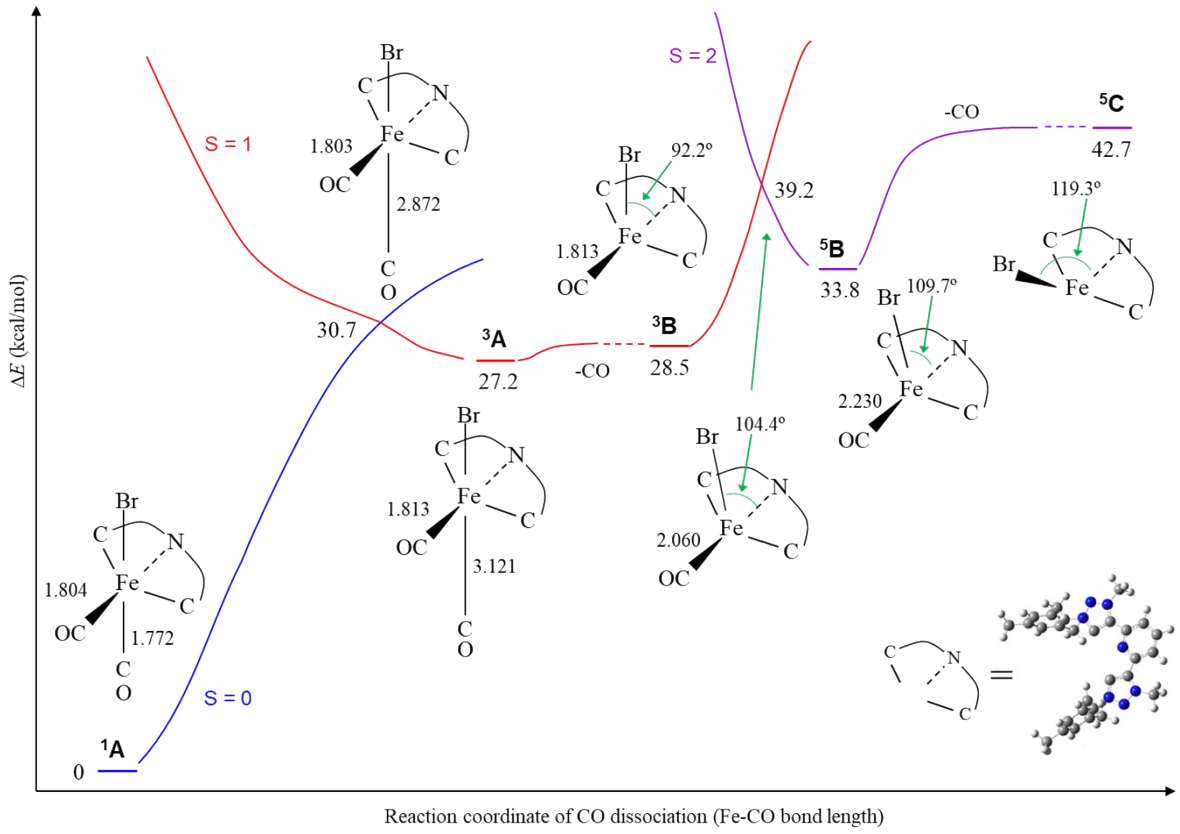

Figure S13. Potential energy curves for minimum-energy path as a function of Fe-CO bond length associated with dissociation of CO ligands from the spin-singlet compound denoted by **^{1}A**. The inserted values indicate the relative energies against the most stable spin-singlet reactant in kcal/mol. Bond lengths of Fe-CO and N−Fe−Br angles in local minimums and transition states are also shown. The broken curves indicate shortened dissociative regions.

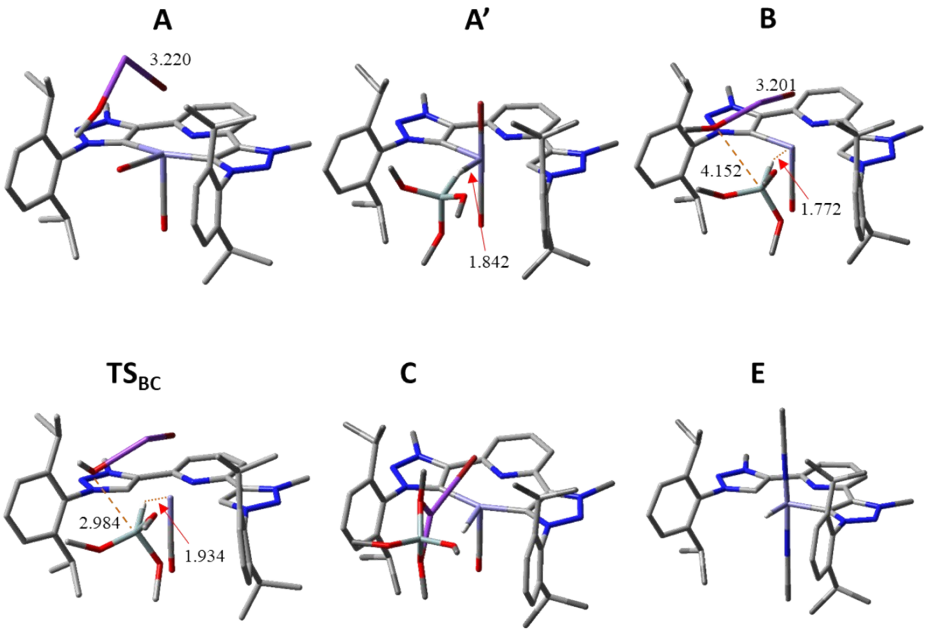

Figure S14. The optimized geometries of local minima and TSs for the transmetallation reaction of $[Fe(MIC)Br(CO)_2]^+$ (**2**) with hydrosilane, calculated with B3LYP/ECP(LanL2DZ) for Fe and 6-31G(d) for others. Hydrogen atoms other than hydrosilane are not displayed for easy viewing of the framework. The inserted values (Å) indicate the interatomic distance between the atoms associated with the reaction.

References

1. H. Iwasaki, Y. Yamada, R. Ishikawa, Y. Koga and K. Matsubara, *Eur. J. Org. Chem.* **2016**, 1651–1654.
2. M. J. Frisch, G. W. Trucks, H. B. Schlegel, et al. *Gaussian 09, Revision D.01*; Gaussian, Inc.: Wallingford CT, 2013.
3. B. Miehlich, A. Savin, H. Stoll, H. Preuss, *Chem. Phys. Lett.* 1989, **157**, 200–206.
4. D. Benito-Garagorri, L. G. Alves, L. F. Veiros, C. M. Standfest-Hauser, S. Tanaka, K. Mereiter and K. Kirchner, *Organometallics* 2010, **29**, 4932–4942.
5. P. J. Hay and W. R. Wadt, *J. Chem. Phys.* 1985, **82**, 270–283.
6. C. Peng, P. Y. Ayala, H. B. Schlegel and M. J. Frisch, *J. Comp. Chem.* 1996, **17**, 49–56.
7. S. Grimme, S. Ehrlich and L. Goerigk, *J. Comp. Chem.* 2011, **32**, 1456–65.
8. J. Tomasi, B. Mennucci and R. Cammi, *Chem. Rev.* 2005, **105**, 2999–3093.

S-5. Products in Catalytic Hydrosilylation

S-5-1. Spectral Data of Isolated, Known Alcohol Products.

1-phenyl-1-ethanol

^{1}H NMR ($CDCl_3$): δ = 7.33-7.39 (m, 3 H, Ph), 7.25-7.30 (m, 2 H, Ph), 4.91 (dq, J = 3.5, 6.4 Hz, 1 H, C*H*CH_3), 1.79 (br, 1 H, OH), 1.50 (d, J = 6.5 Hz, 3 H, CHCH_3); ^{13}C NMR ($CDCl_3$): δ = 145.76 (Ph, 4°), 128.31 (Ph), 127.25 (Ph), 125.30 (Ph), 70.12 (*C*HCH_3), 24.99 (CH*C*H_3).

1-(4'-bromo)phenyl-1-ethanol

^{1}H NMR ($CDCl_3$): δ = 7.47 (d, J = 8.4 Hz, 2 H, Ph), 7.25 (d, J = 8.4 Hz, 2 H, Ph), 4.87 (dq, J = 3.2, 6.4 Hz, 1 H, C*H*CH_3), 1.80 (d, J = 3.2 Hz, 1 H, OH), 1.47 (d, J = 6.4 Hz, 3 H, CHCH_3); ^{13}C NMR ($CDCl_3$): δ = 144.67 (Ph, 4°), 131.37 (Ph), 127.05 (Ph), 120.94 (Ph, 4°), 69.49 (*C*HCH_3), 25.05 (CH*C*H_3).

1-(4'-trifluoromethyl)phenyl-1-ethanol

^{1}H NMR ($CDCl_3$): δ = 7.61 (d, J = 8.4 Hz, 2 H, Ph), 7.49 (d, J = 8.4 Hz, 2 H, Ph), 4.97 (dq, J = 3.2, 6.4 Hz, 1 H, C*H*CH_3), 1.87 (d, J = 3.2 Hz, 1 H, OH), 1.51 (d, J = 6.4 Hz, 3 H, CHCH_3); ^{13}C NMR ($CDCl_3$): δ = 149.67 (Ph, 4°), 129.52 (q, J_{CF} = 84 Hz, Ph, 4°), 125.60 (Ph), 125.31 (q, J = 3.7 Hz, Ph), 124.15 (q, J = 270 Hz, CF_3), 69.63 (*C*HCH_3), 25.11 (CH*C*H_3); ^{19}F NMR ($CDCl_3$): δ = -62.50.

1-(2'-bromo)phenyl-1-ethanol

^{1}H NMR ($CDCl_3$): δ = 7.60 (dd, J = 1.6, 7.6 Hz, 1 H, Ph), 7.51 (dd, J = 1.6, 7.6 Hz, 1 H, Ph), 7.35 (dt, J = 1.1, 7.6 Hz, 1 H, Ph), 7.13 (dt, J = 1.6, 7.6 Hz, 1 H, Ph), 5.25 (dq, J = 3.2, 6.4 Hz, 1 H, C*H*CH_3), 1.97 (d, J = 3.5 Hz, 1 H, OH), 1.49 (d, J = 6.4 Hz, 3 H, CHCH_3); ^{13}C NMR ($CDCl_3$): δ = 144.61 (Ph, 4°), 132.57 (Ph), 128.66 (Ph), 127.77 (Ph), 121.63 (Ph), 121.62 (Ph, 4°), 69.08 (*C*HCH_3), 23.53 (CH*C*H_3).

(4-methylphenyl)methanol

^{1}H NMR ($CDCl_3$): δ = 7.26 (d, J = 8.0 Hz, 2 H, Ph), 7.17 (d, J = 8.0 Hz, 2 H, Ph), 4.65 (brs, 2 H, CH_2), 2.36 (s, 3 H, CH_3), 1.67 (br, 1 H, OH); ^{13}C NMR ($CDCl_3$): δ = 137.85 (Ph, 4°), 136.99 (Ph, 4°), 128.99 (Ph), 126.95 (Ph), 64.70 (CH_2), 20.96 (CH_3).

benzylalcohol

^{1}H NMR ($CDCl_3$): δ = 7.36-7.37 (m, 4 H, Ph), 7.28-7.33 (m, 1 H, Ph), 4.70 (d, J = 5.9 Hz, 2 H, CH_2), 1.65 (t, J = 5.9 Hz, 1 H, OH); ^{13}C NMR ($CDCl_3$): δ = 140.78 (Ph, 4°), 128.39 (Ph), 127.44 (Ph), 126.88 (Ph), 64.94 (CH_2).

4'-methoxybenzylalcohol

^{1}H NMR ($CDCl_3$): δ = 7.29 (d, J = 8.8 Hz, 2 H, Ph), 6.89 (d, J = 8.8 Hz, 2 H, Ph), 4.62 (brs, 2 H, CH_2), 3.81 (s, 3 H, CH_3), 1.65 (br, 1 H, OH); ^{13}C NMR ($CDCl_3$): δ = 158.90 (Ph, 4°), 133.10 (Ph, 4°), 128.42 (Ph), 113.72 (Ph), 64.48 (CH_2), 55.08 (CH_3).

4'-trifluoromethylbenzylalcohol

^{1}H NMR ($CDCl_3$): δ = 7.61 (d, J = 8.0 Hz, 2 H, Ph), 7.47 (d, J = 8.0 Hz, 2 H, Ph), 4.76 (s, 2 H, CH_2), 1.98 (brs, 1 H, OH); ^{13}C NMR ($CDCl_3$): δ = 144.62 (Ph, 4°), 129.65 (q, J_{CF} = 32 Hz, Ph, 4°), 126.73 (Ph), 125.31 (q, J = 3.8 Hz, Ph), 124.12 (q, J = 270 Hz, CF_3), 64.08 (CH_2); ^{19}F NMR ($CDCl_3$): δ = -62.50.

4'-bromobenzylalcohol

^{1}H NMR ($CDCl_3$): δ = 7.49 (d, J = 8.0 Hz, 2 H, Ph), 7.25(d, J = 8.0 Hz, 2 H, Ph), 4.66 (s, 2 H, CH_2), 1.65 (br, 1 H, OH); ^{13}C NMR ($CDCl_3$): δ = 139.62 (Ph, 4°), 131.42 (Ph), 128.44 (Ph), 121.22 (Ph, 4°), 64.12 (CH_2).

2'-fluorobenzylalcohol

^{1}H NMR ($CDCl_3$): δ = 7.43 (dt, J = 1.6, 7.6 Hz, 1 H, Ph), 7.27-7.31 (m, 1 H, Ph), 7.15 (dt, J = 1.6, 7.6 Hz, 1 H, Ph), 7.05 (t, J = 8.8 Hz, 1 H, Ph), 4.77 (s, 1 H, CH_2), 1.76 (br, 1 H, OH); ^{13}C NMR ($CDCl_3$): δ = 160.49 (d, J_{CF} = 246 Hz, Ph, 4°), 129.21 (d, J_{CF} = 2.2 Hz, Ph), 129.15 (Ph), 127.75 (d, J_{CF} = 14.7 Hz, Ph), 124.11 (d, J_{CF} = 3.3 Hz, Ph), 115.11 (d, J_{CF} = 21.8 Hz, Ph), 58.99 (d, JCF = 4.3 Hz, CH_3); ^{19}F NMR ($CDCl_3$): δ = -119.83.

S-5-2. ^{1}H NMR Detection of Silylethers in Hydrosilylation.

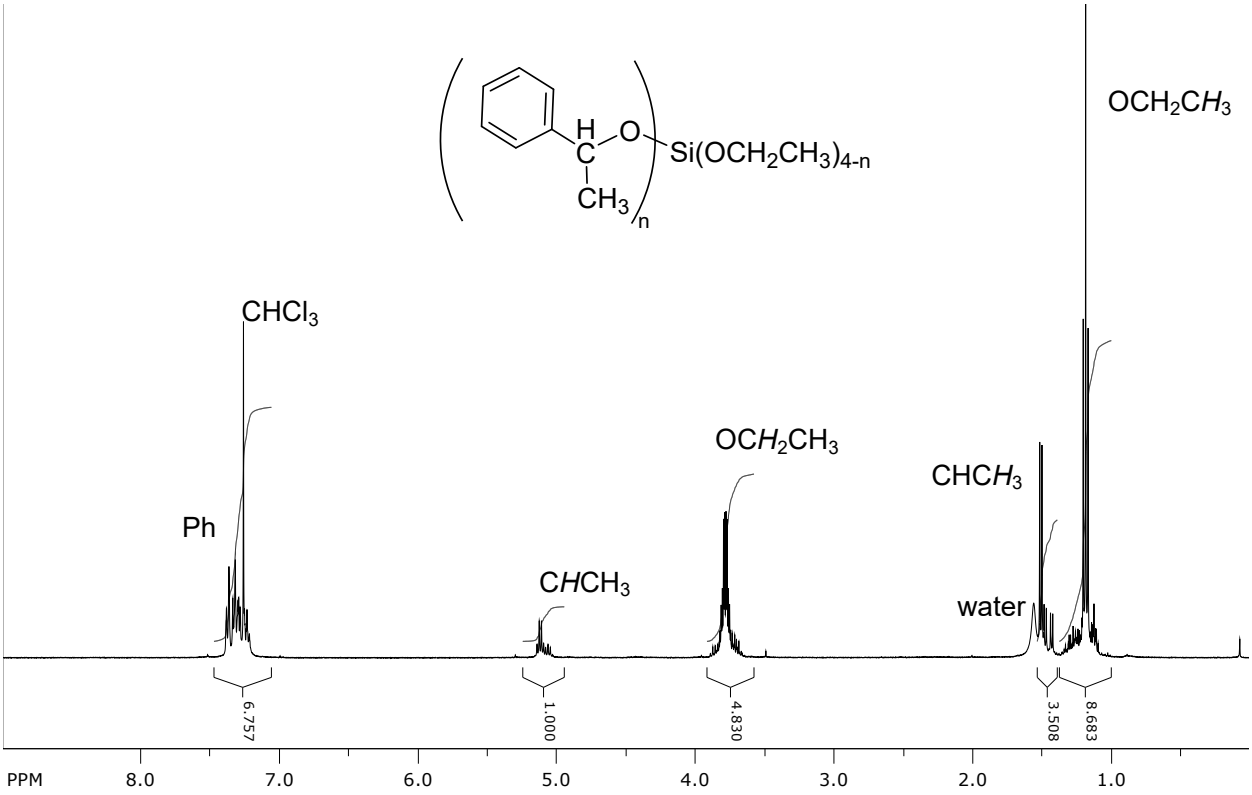

Figure S15. ^{1}H NMR spectrum of the product mixture of silylethers, (1-phenyl-1-ethoxy)$_n$Si(OEt)$_{4-n}$ after hydrosilylation of acetophenone with HSi(OEt)$_3$ ($CDCl_3$, 400Hz).

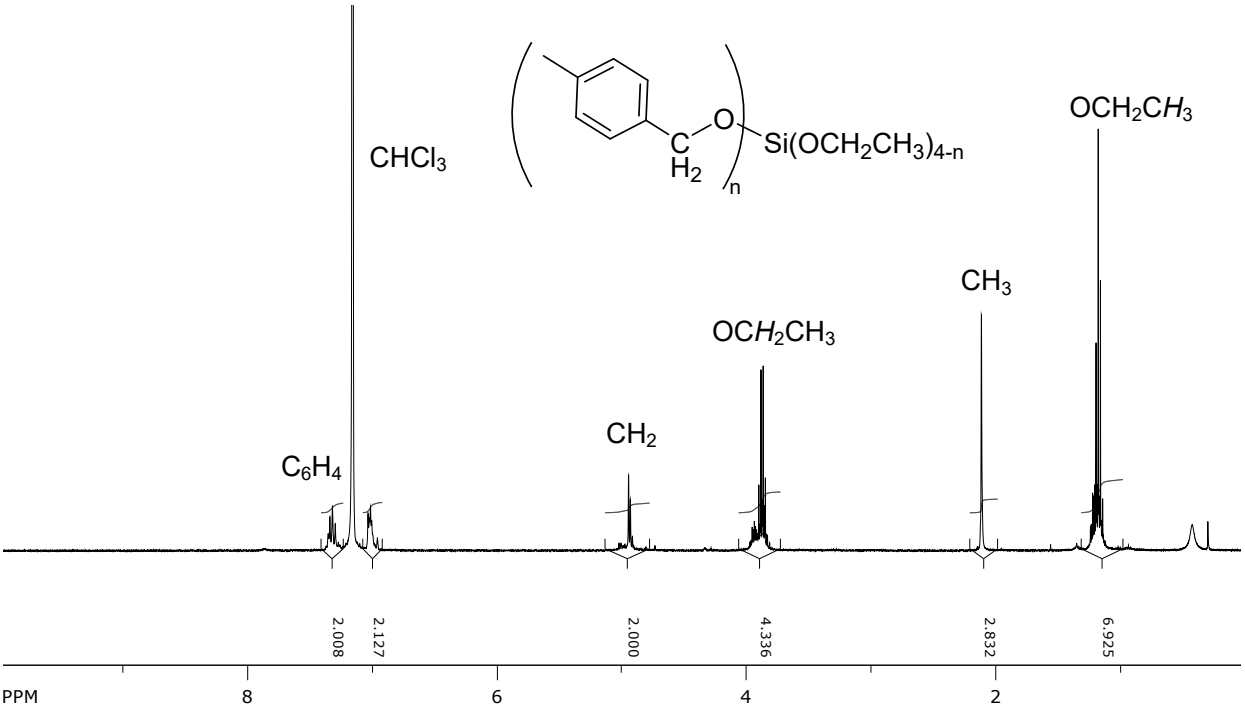

Figure S16. ^{1}H NMR spectrum of the product mixture of silylethers, (4-methylbenzyl)$_n$Si(OEt)$_{4-n}$ after hydrosilylation of 4'-methylbenzaldehyde with HSi(OEt)$_3$ ($CDCl_3$, 400Hz).

S-5-3. NMR Spectra of the Products in Hydrosilylationa

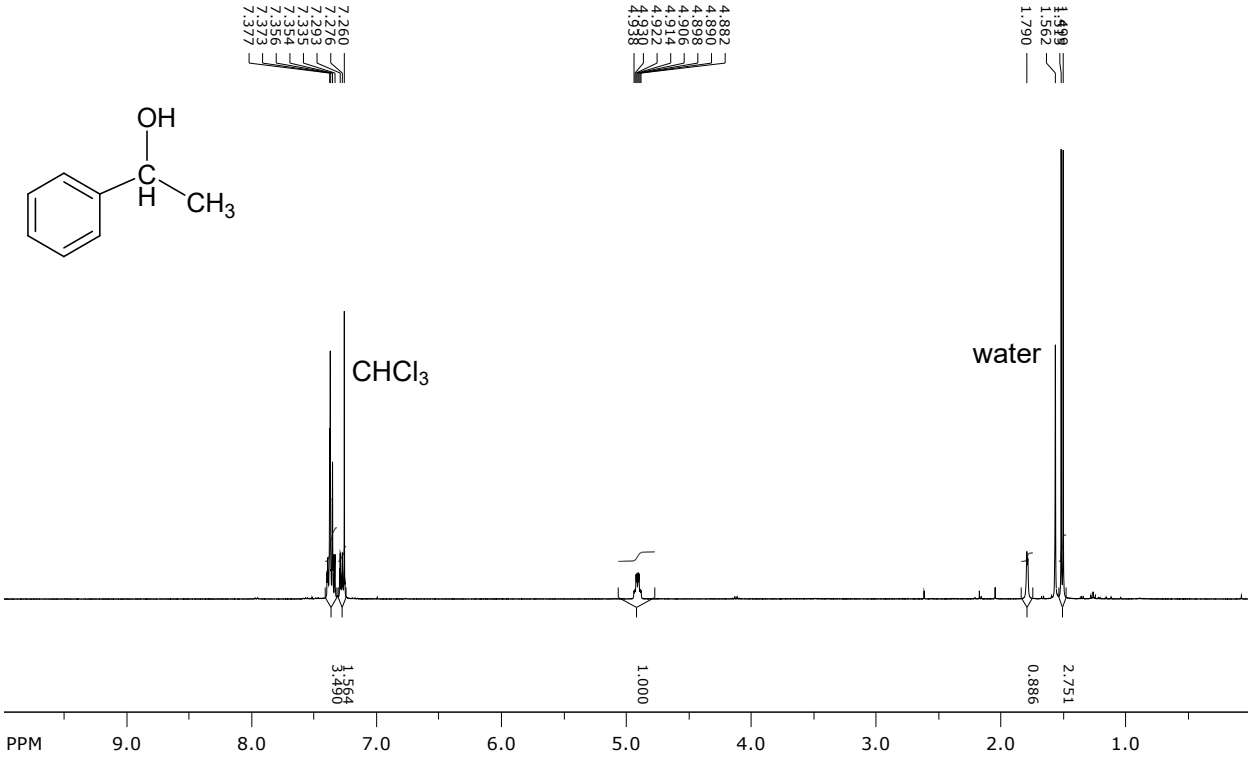

Figure S17. ^{1}H NMR spectrum of 1-phenyl-1-ethanol ($CDCl_3$, 400Hz).

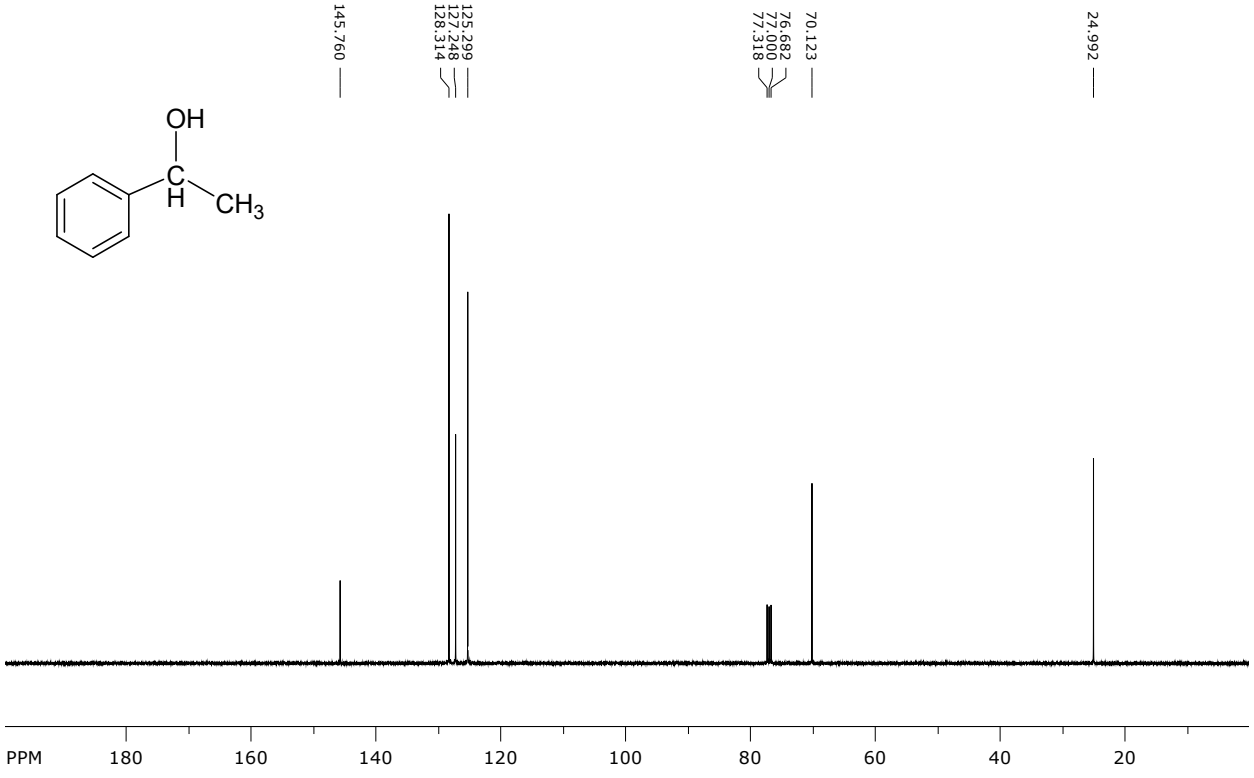

Figure S18. ^{13}C NMR spectrum of 1-phenyl-1-ethanol ($CDCl_3$, 100Hz).

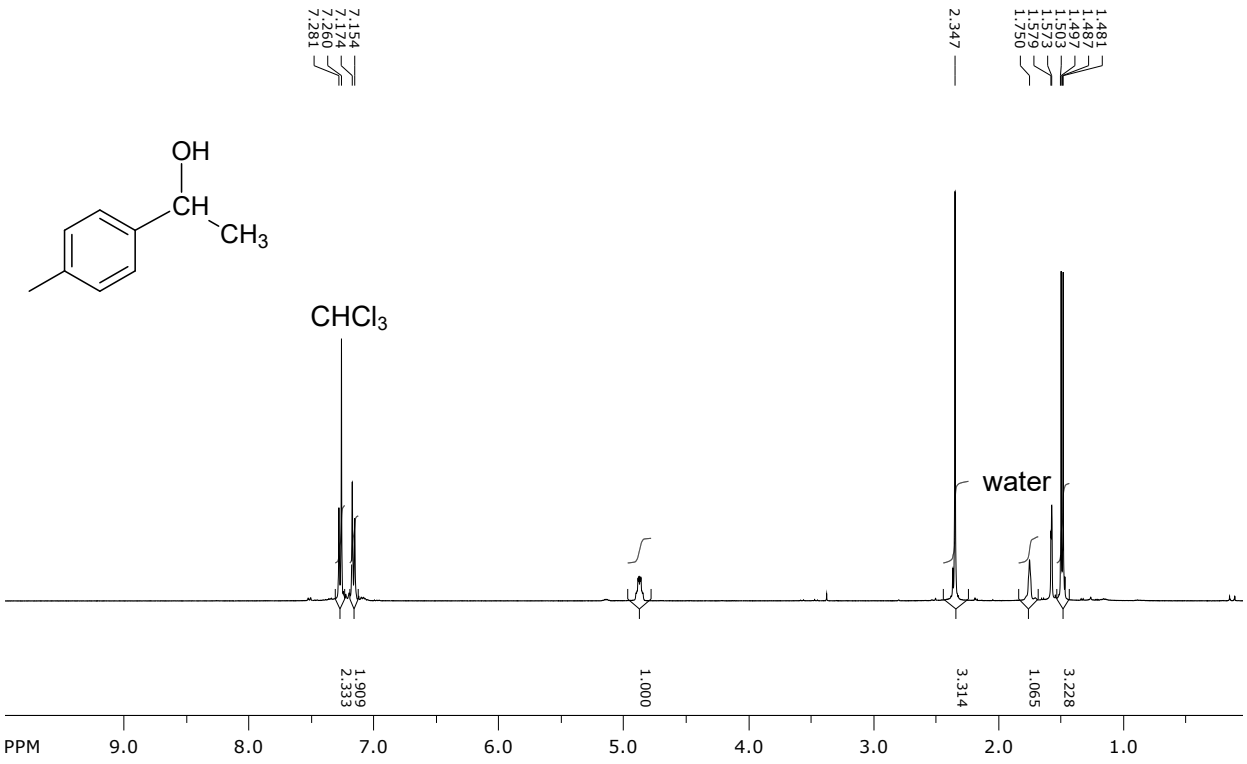

Figure S19. ^{1}H NMR spectrum of 1-(4'-methyl)phenyl-1-ethanol ($CDCl_3$, 400Hz).

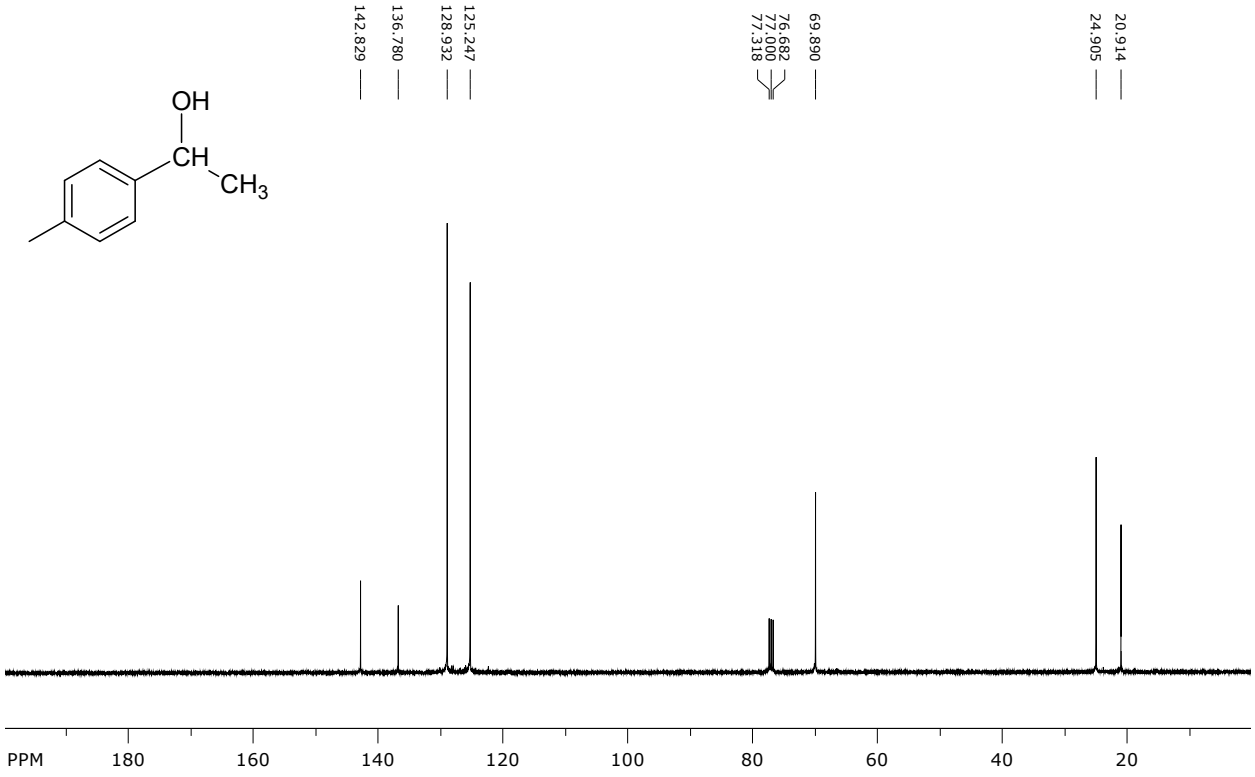

Figure S20. ^{13}C NMR spectrum of 1-(4'-methyl)phenyl-1-ethanol ($CDCl_3$, 100Hz).

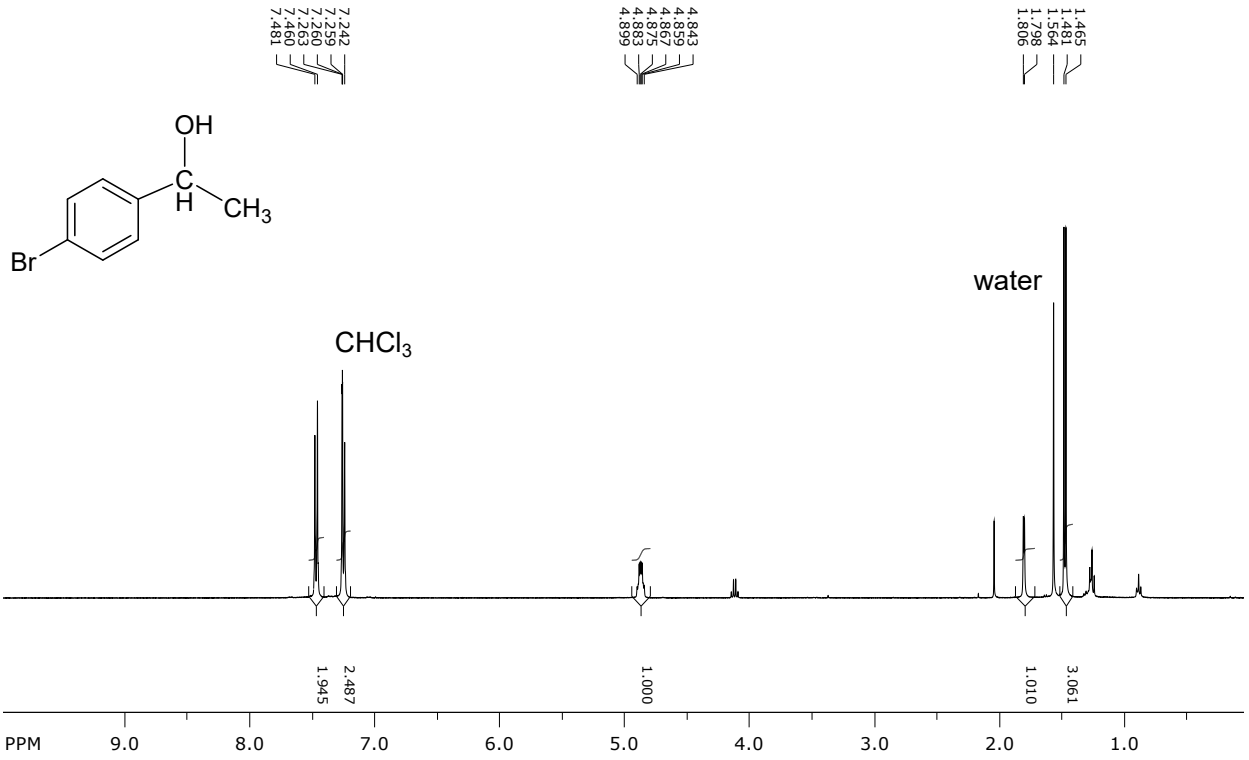

Figure S21. ^{1}H NMR spectrum of 1-(4'-bromo)phenyl-1-ethanol ($CDCl_3$, 400Hz).

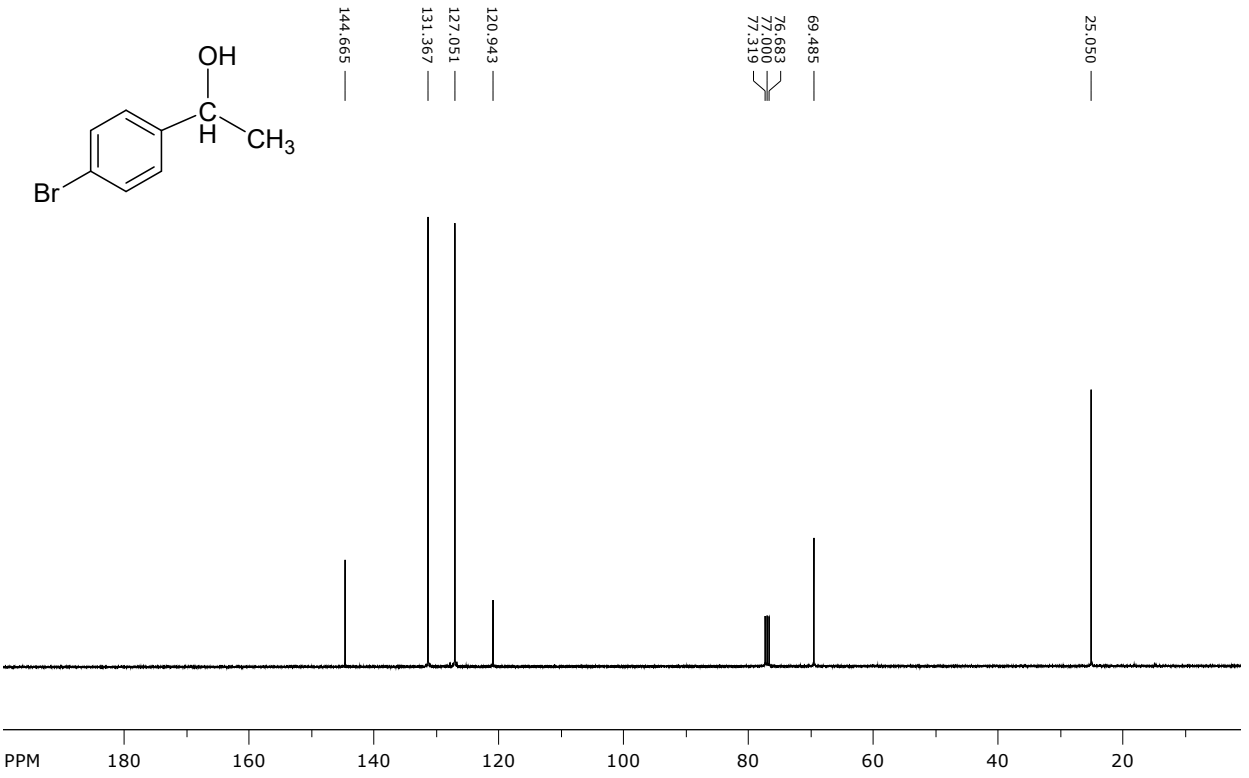

Figure S22. ^{13}C NMR spectrum of 1-(4'-bromo)phenyl-1-ethanol ($CDCl_3$, 100Hz).

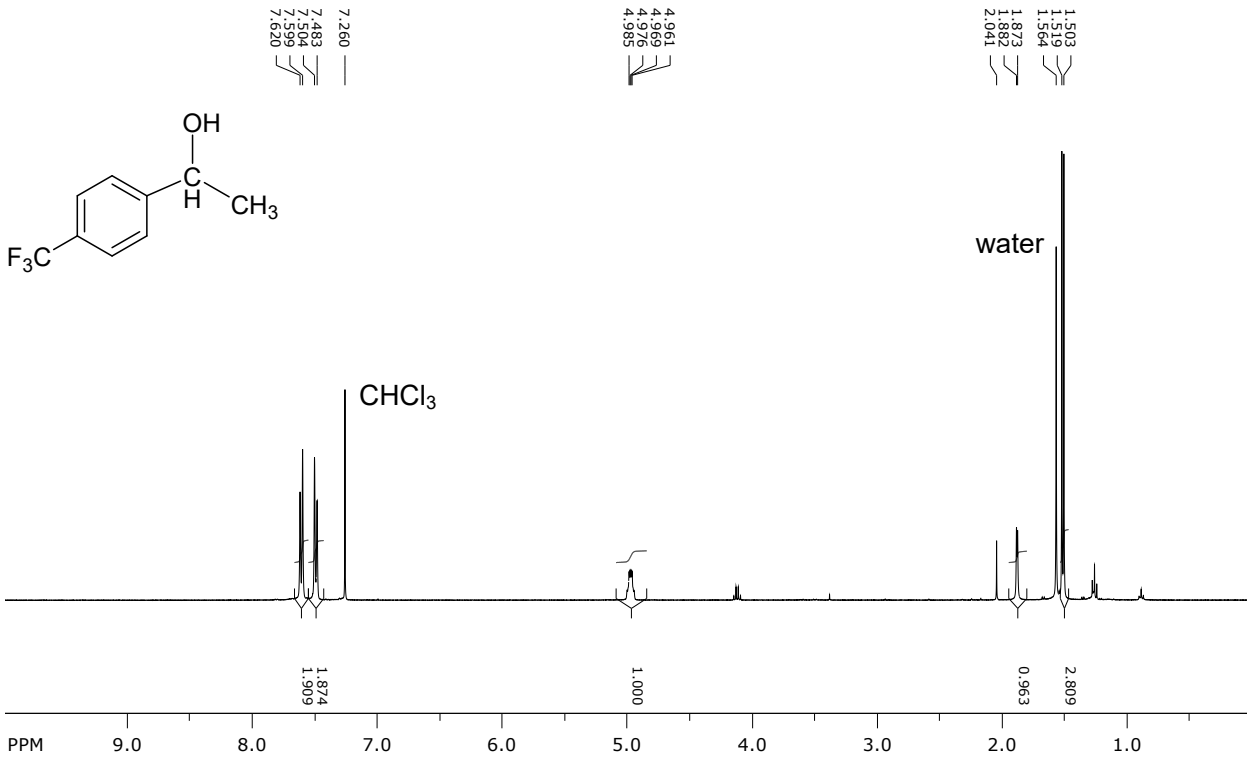

Figure S23. ^{1}H NMR spectrum of 1-(4-trifluoromethyl)phenyl-1-ethanol ($CDCl_3$, 400Hz).

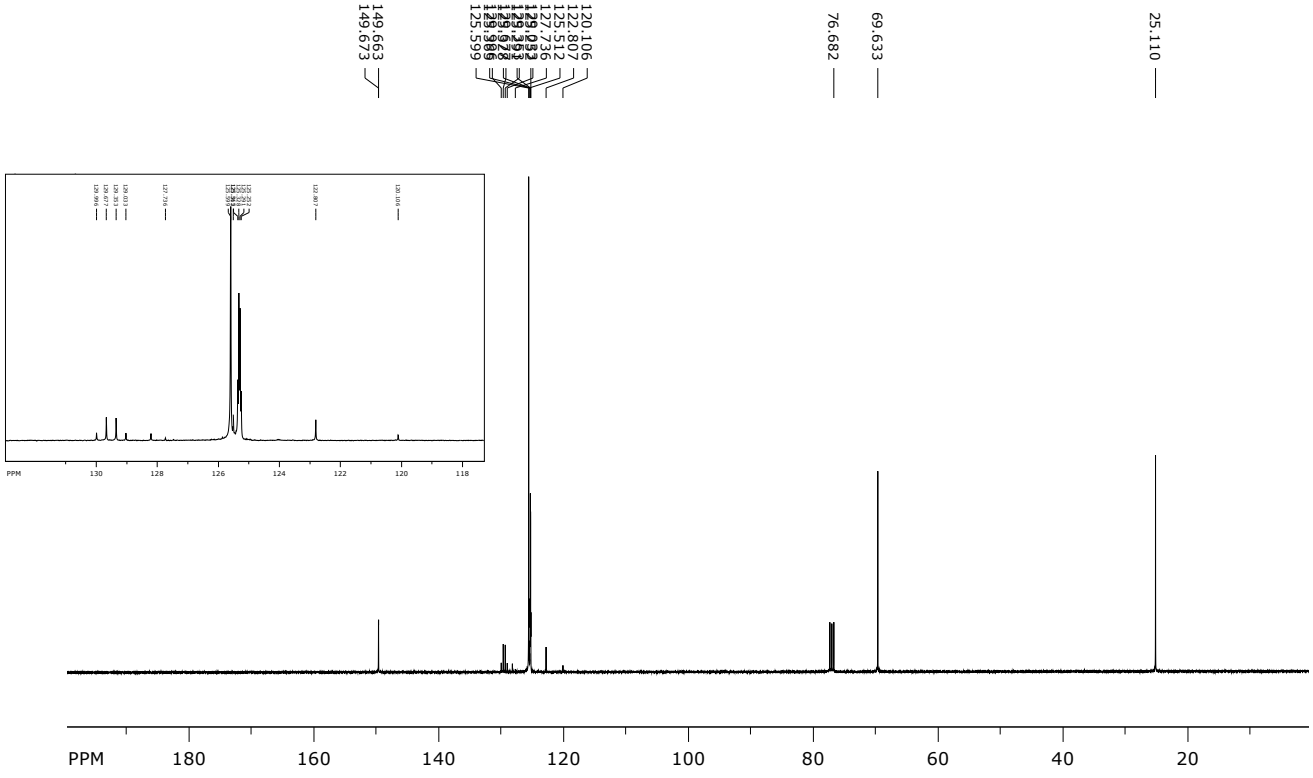

Figure S24. ^{13}C NMR spectrum of 1-(4'-trifluoromethyl)phenyl-1-ethanol ($CDCl_3$, 100Hz). The superimposed spectrum corresponds to the area of the aromatic carbons.

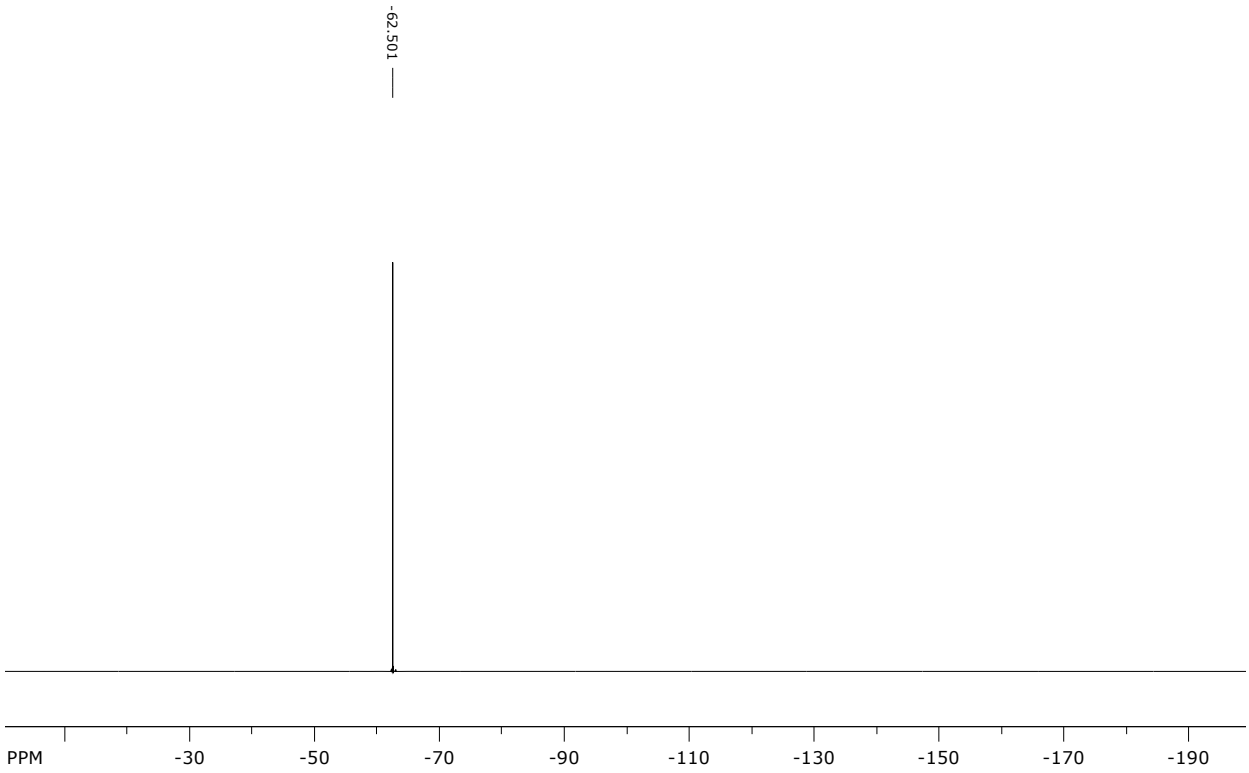

Figure S25. ^{19}F NMR spectrum of 1-(4'-trifluoromethyl)phenyl-1-ethanol ($CDCl_3$, 376 MHz).

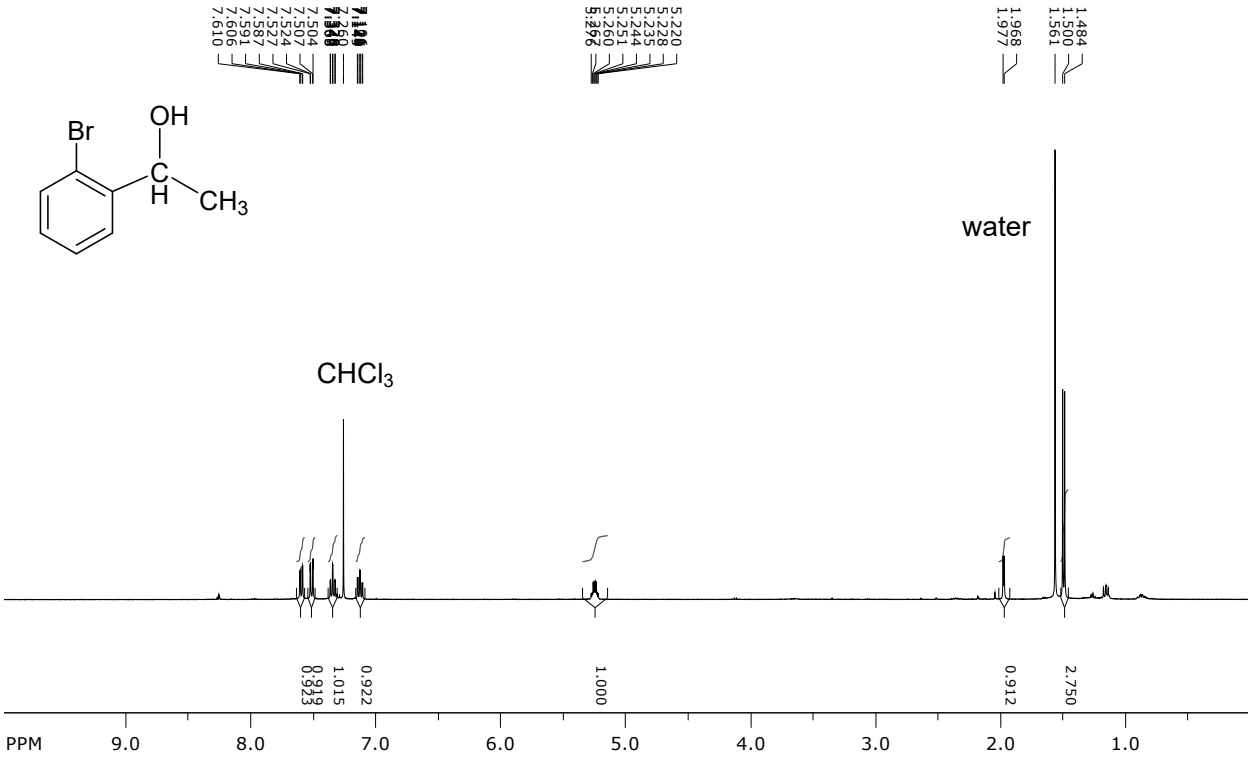

Figure S26. ^{1}H NMR spectrum of 1-(2'-bromo)phenyl-1-ethanol ($CDCl_3$, 400Hz).

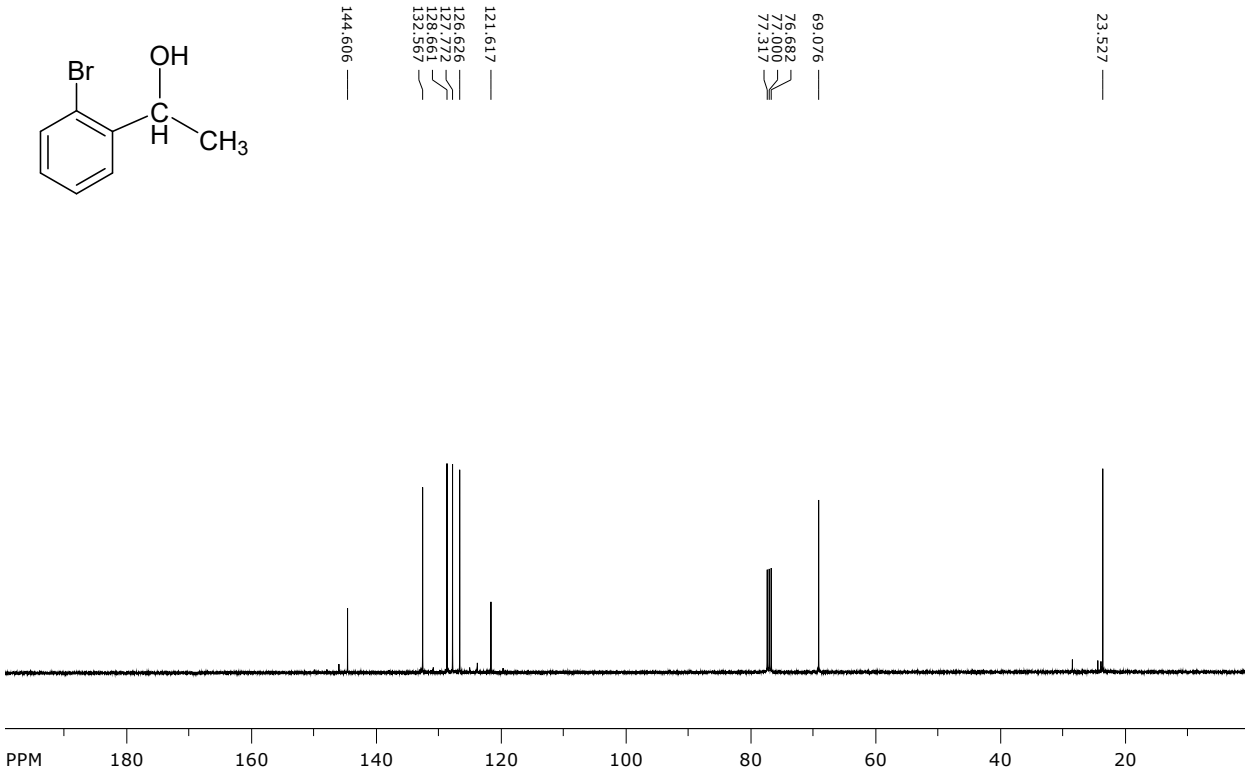

Figure S27. ^{13}C NMR spectrum of 1-(2'-bromo)phenyl-1-ethanol ($CDCl_3$, 100Hz).

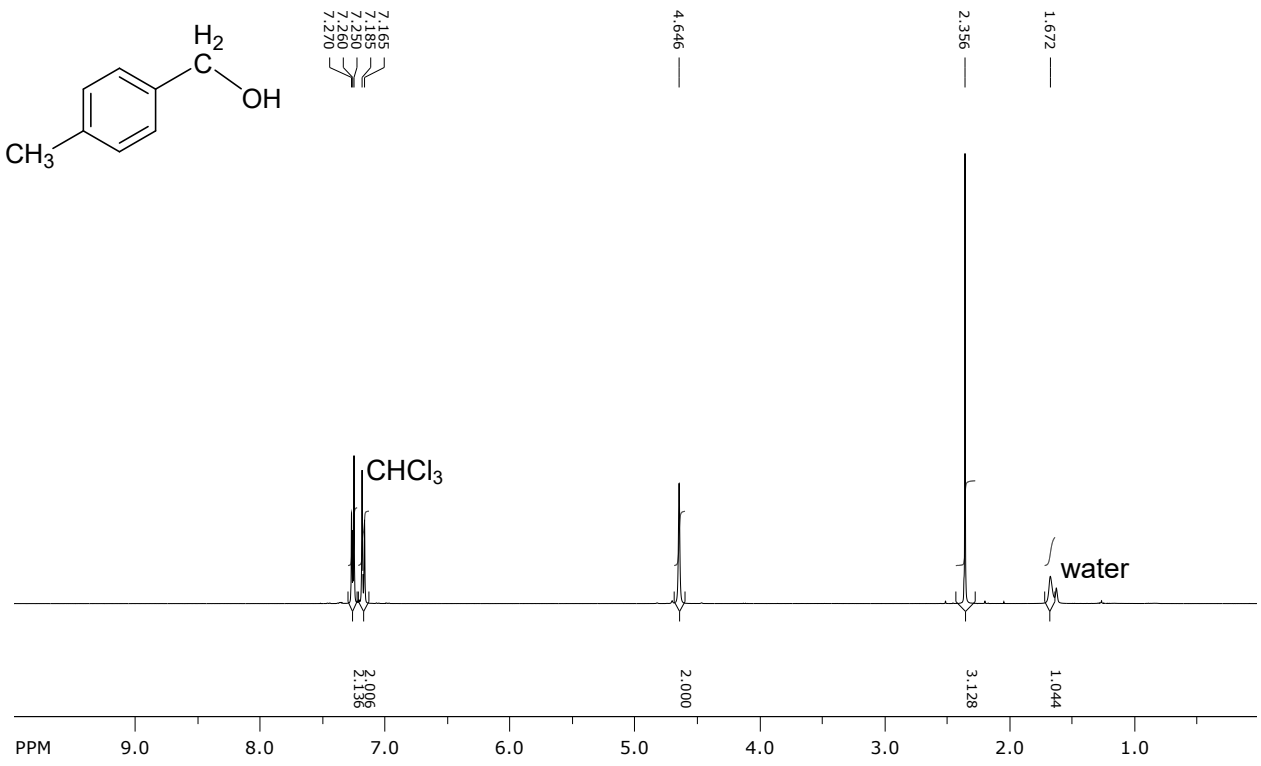

Figure S28. ^{1}H NMR spectrum of 4'-methylbenzylalcohol ($CDCl_3$, 400Hz).

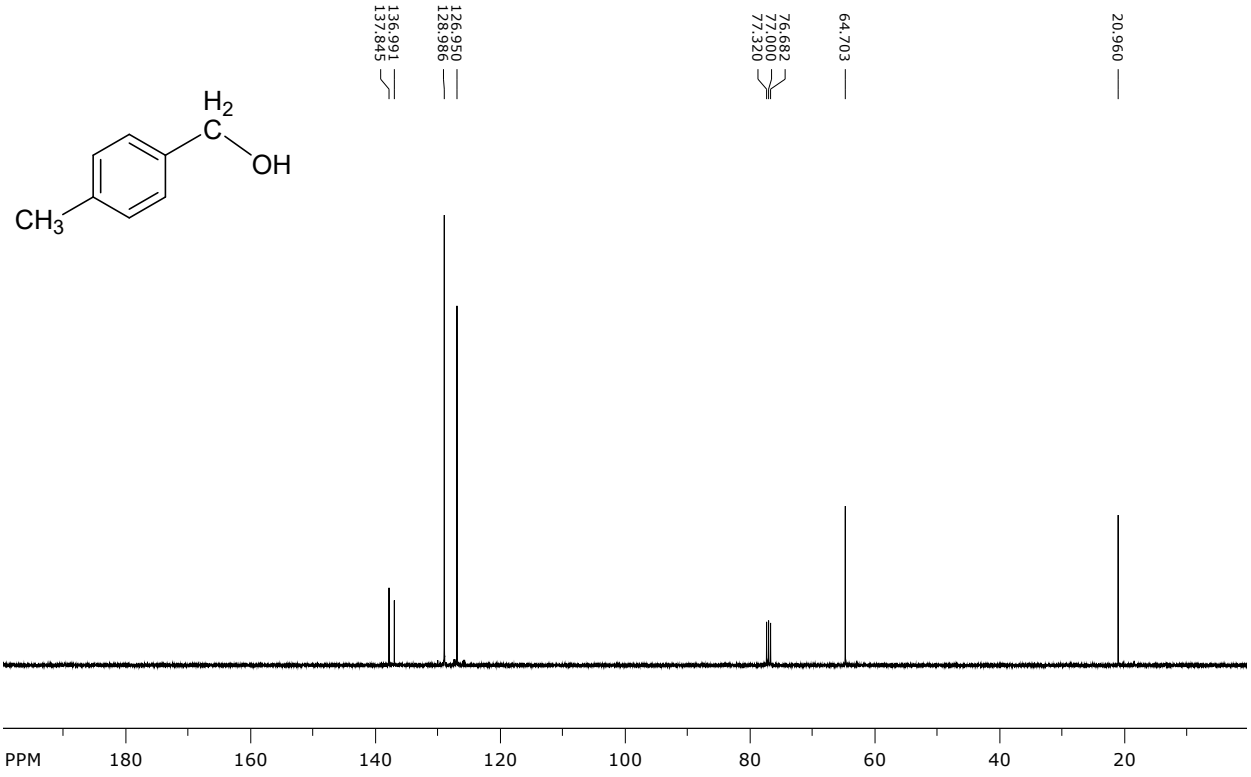

Figure S29. ^{13}C NMR spectrum of 4'-methylbenzylalcohol ($CDCl_3$, 100Hz).

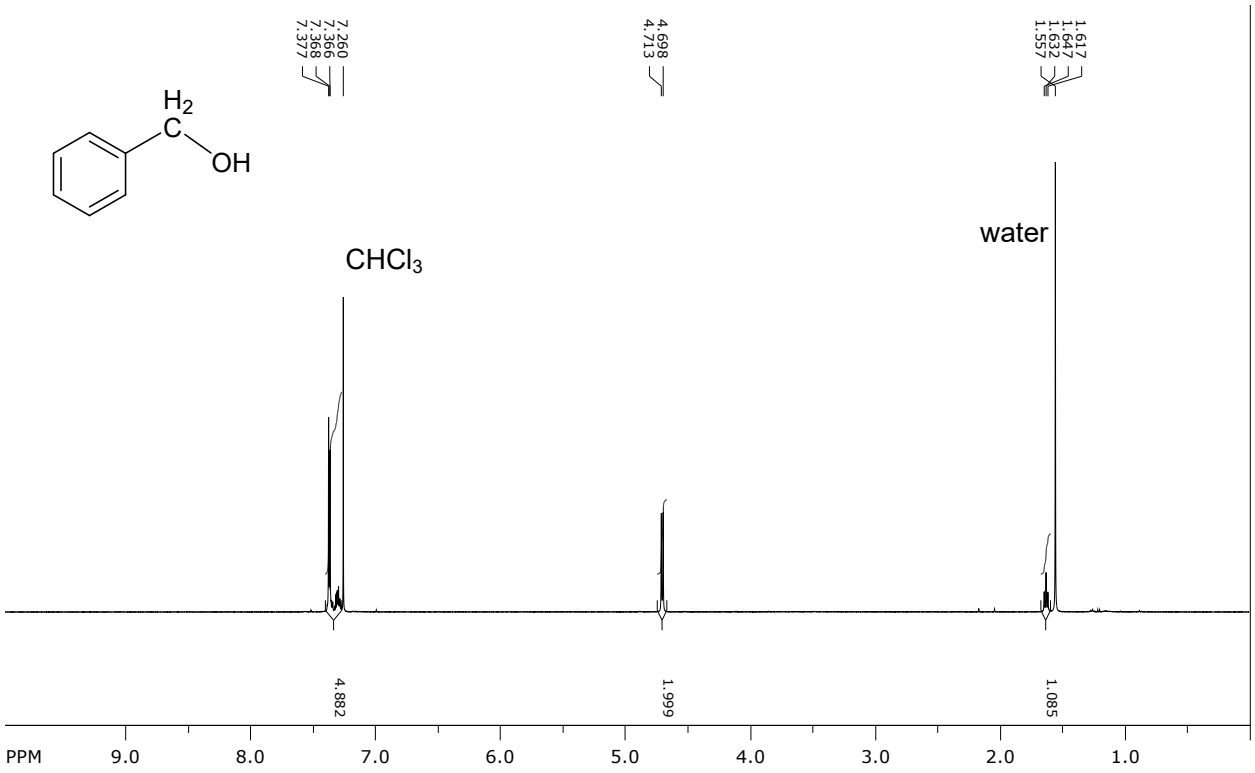

Figure S30. ^{1}H NMR spectrum of benzylalcohol ($CDCl_3$, 400Hz).

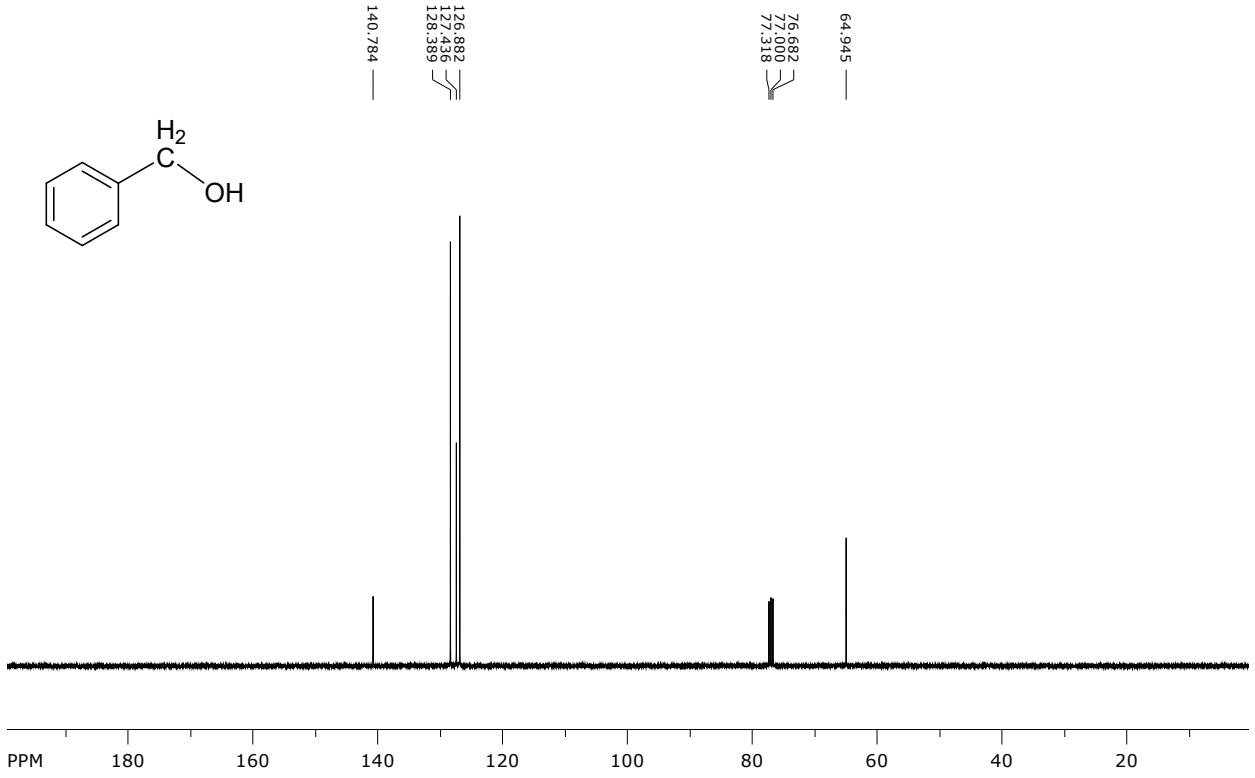

Figure S31. ^{13}C NMR spectrum of benzylalcohol ($CDCl_3$, 100Hz).

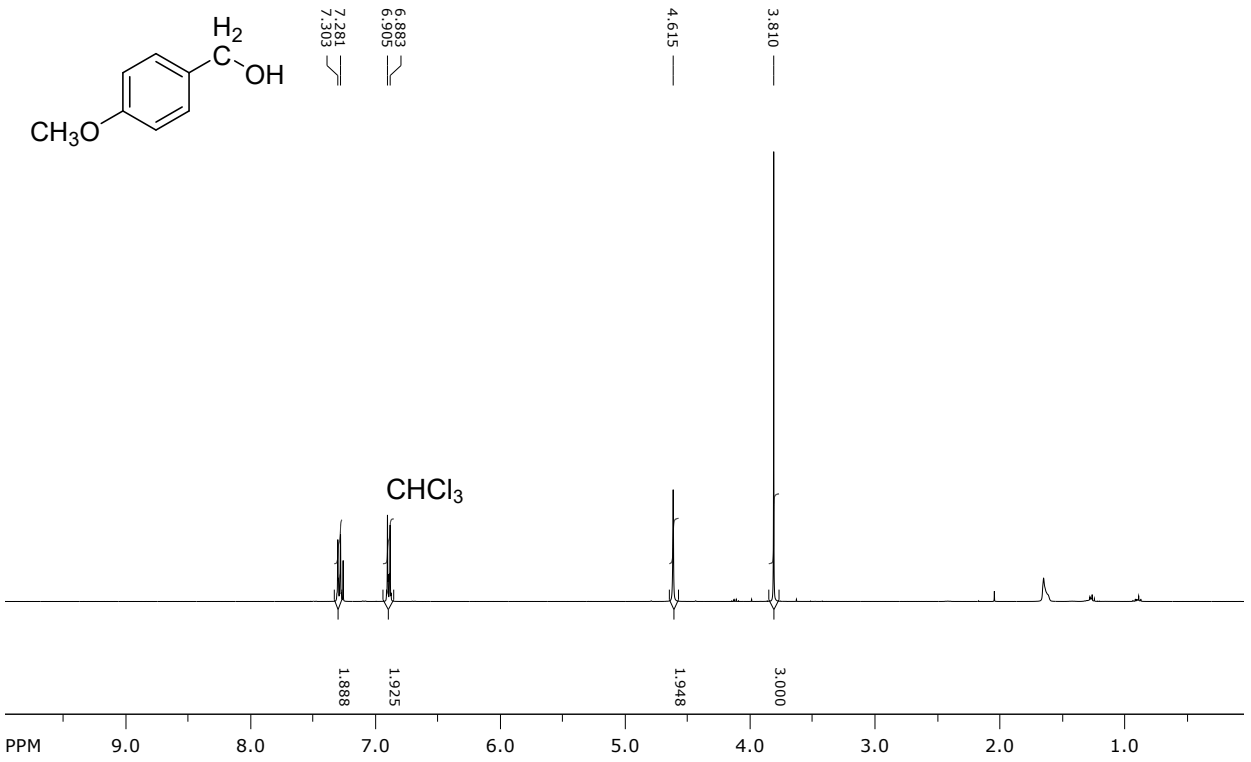

Figure S32. ^{1}H NMR spectrum of 4'-methoxybenzylalcohol ($CDCl_3$, 400Hz).

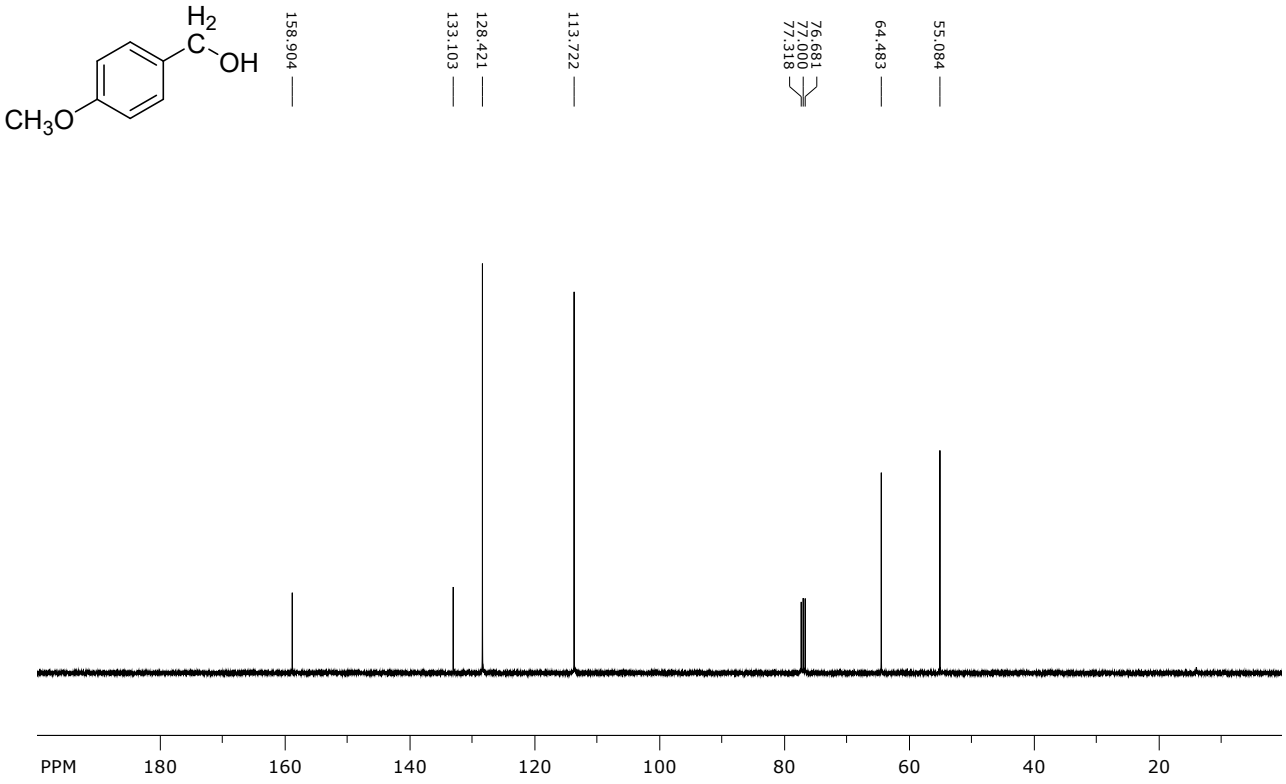

Figure S33. ^{13}C NMR spectrum of 4'-methoxybenzylalcohol ($CDCl_3$, 100Hz).

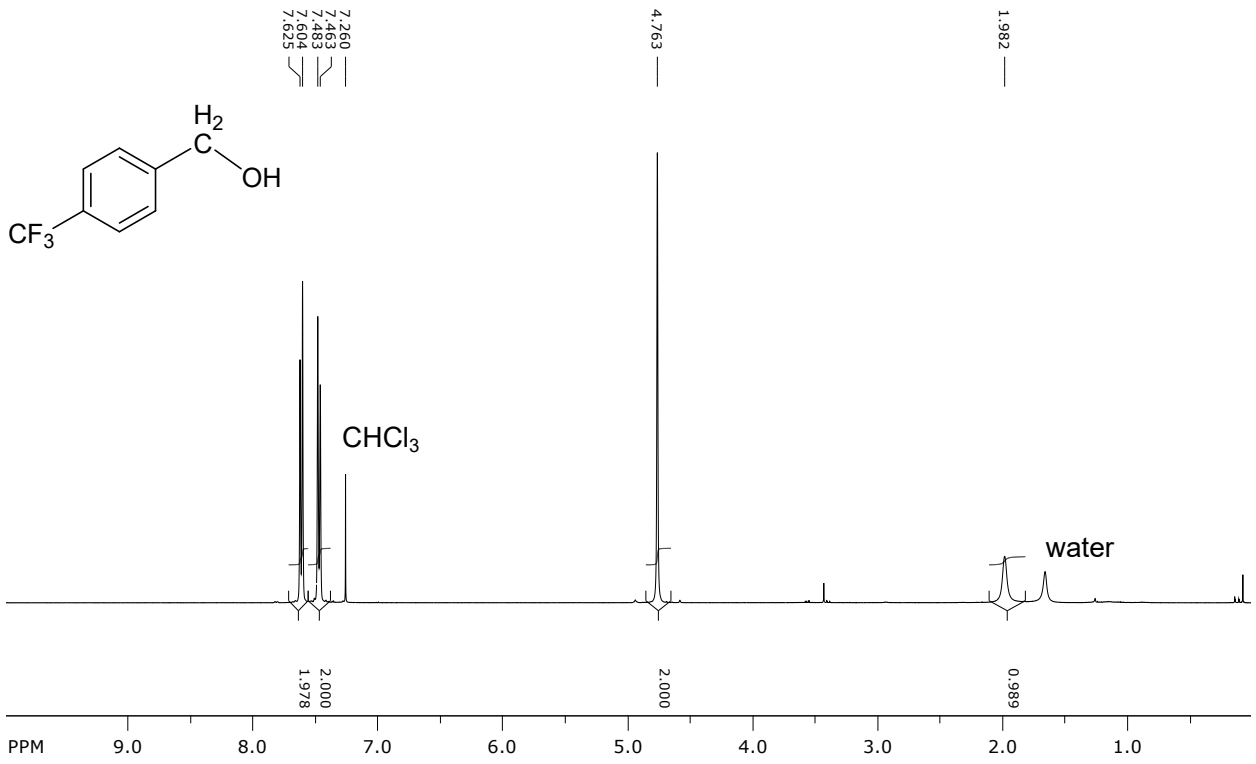

Figure S34. ^{1}H NMR spectrum of 4'-trifluoromethylbenzylalcohol ($CDCl_3$, 400Hz).

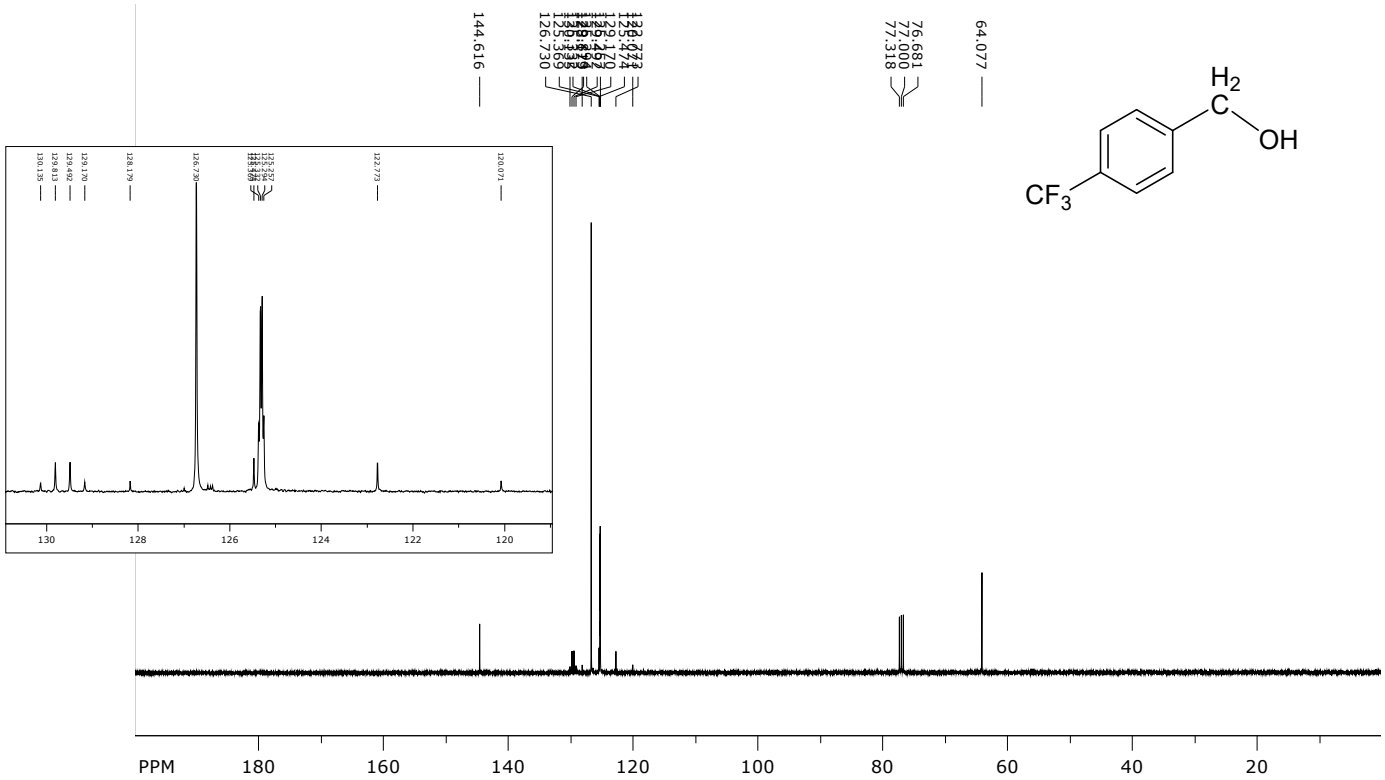

Figure S35. ^{13}C NMR spectrum of 4'-trifluoromethylbenzylalcohol ($CDCl_3$, 100Hz). The superimposed spectrum corresponds to the area of the aromatic carbons.

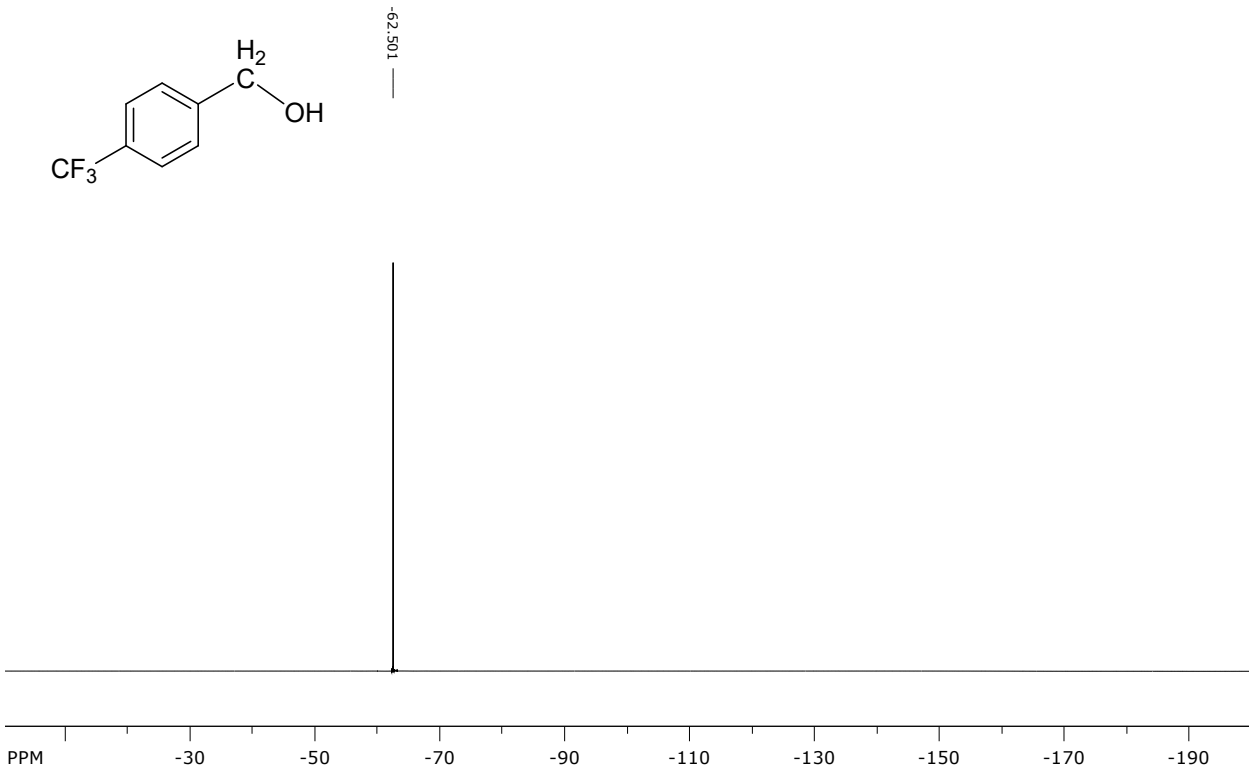

Figure S36. ^{19}F NMR spectrum of 4'-trifluoromethylbenzylalcohol ($CDCl_3$, 376 MHz).

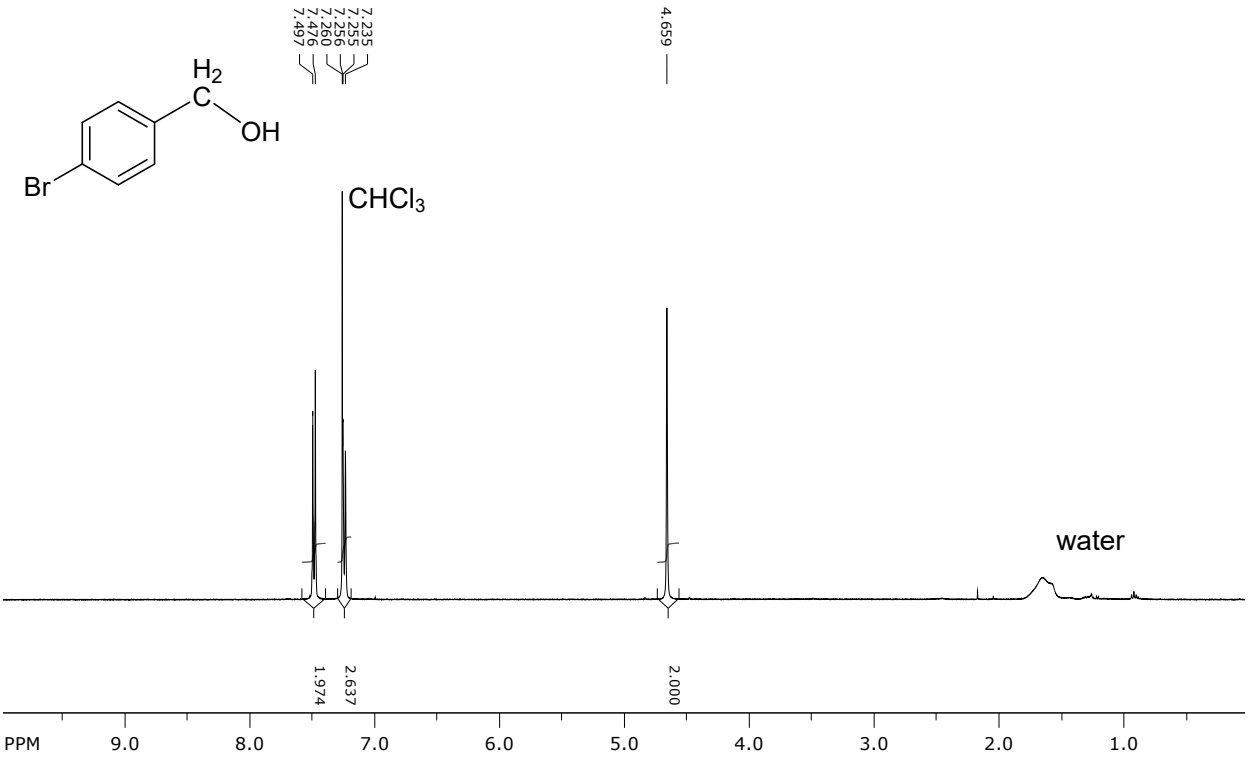

Figure S37. ^{1}H NMR spectrum of 4'-bromobenzylalcohol ($CDCl_3$, 400Hz).

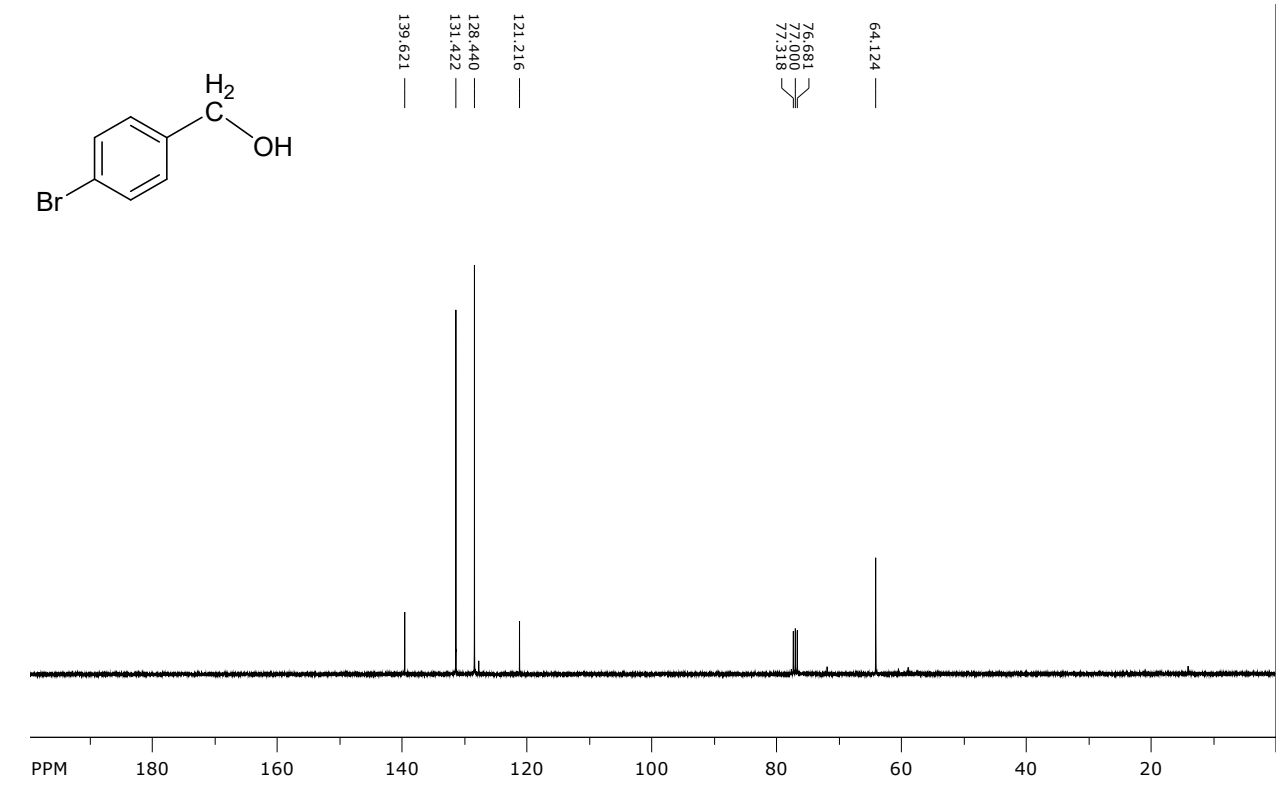

Figure S38. ^{13}C NMR spectrum of 4'-bromobenzylalcohol ($CDCl_3$, 100Hz).

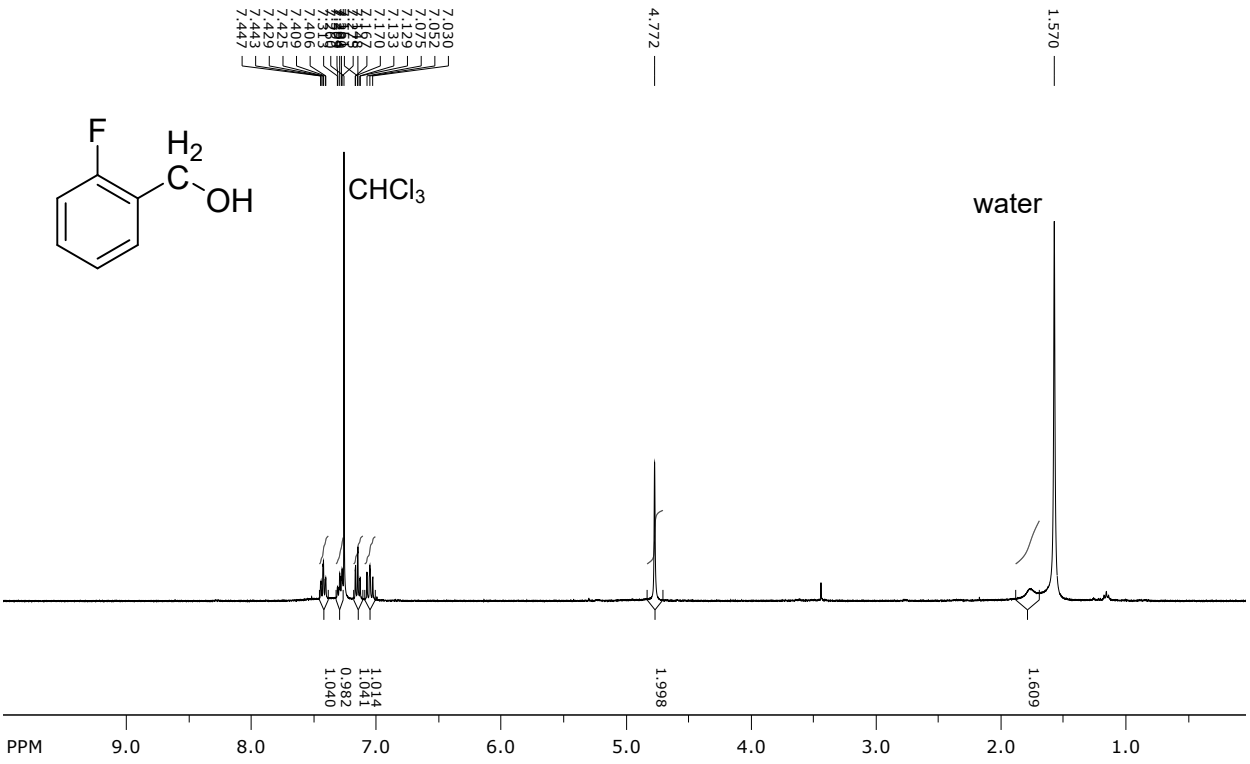

Figure S39. ^{1}H NMR spectrum of 2'-fluorobenzylalcohol ($CDCl_3$, 400Hz).

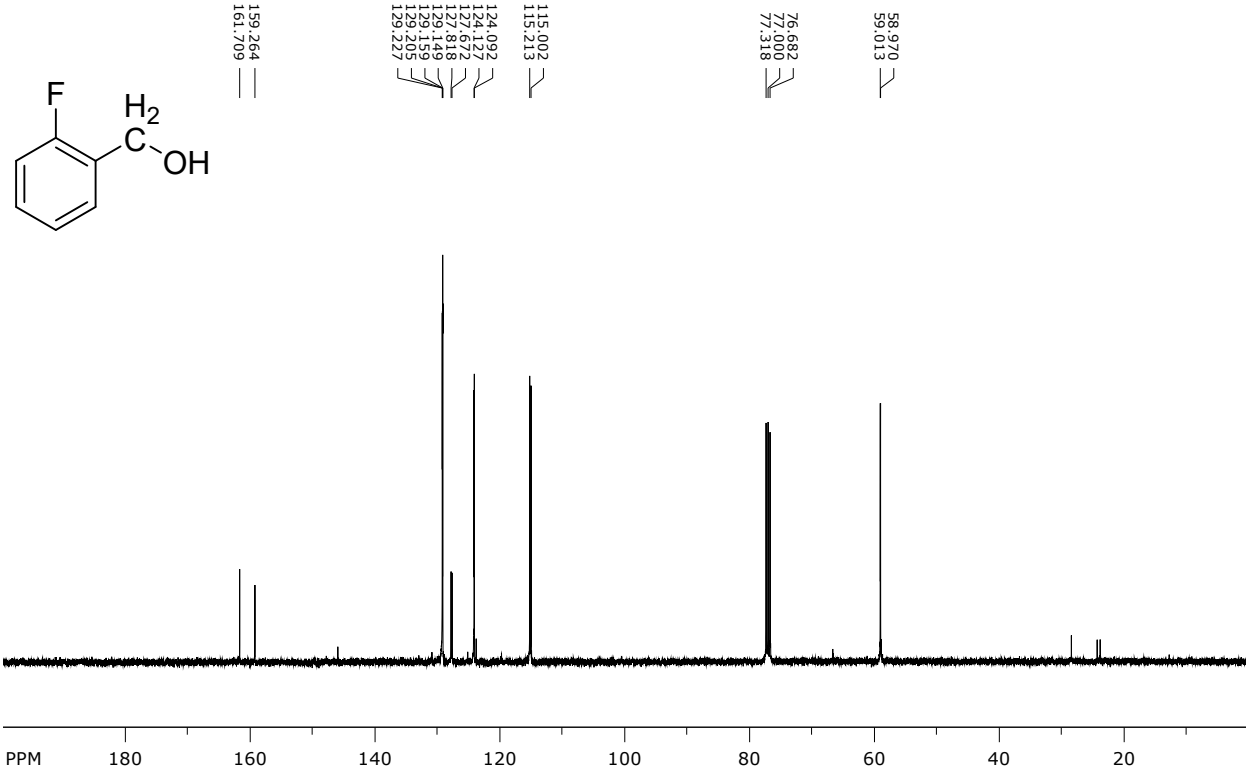

Figure S40. ^{13}C NMR spectrum of 2'-fluorobenzylalcohol ($CDCl_3$, 100Hz).

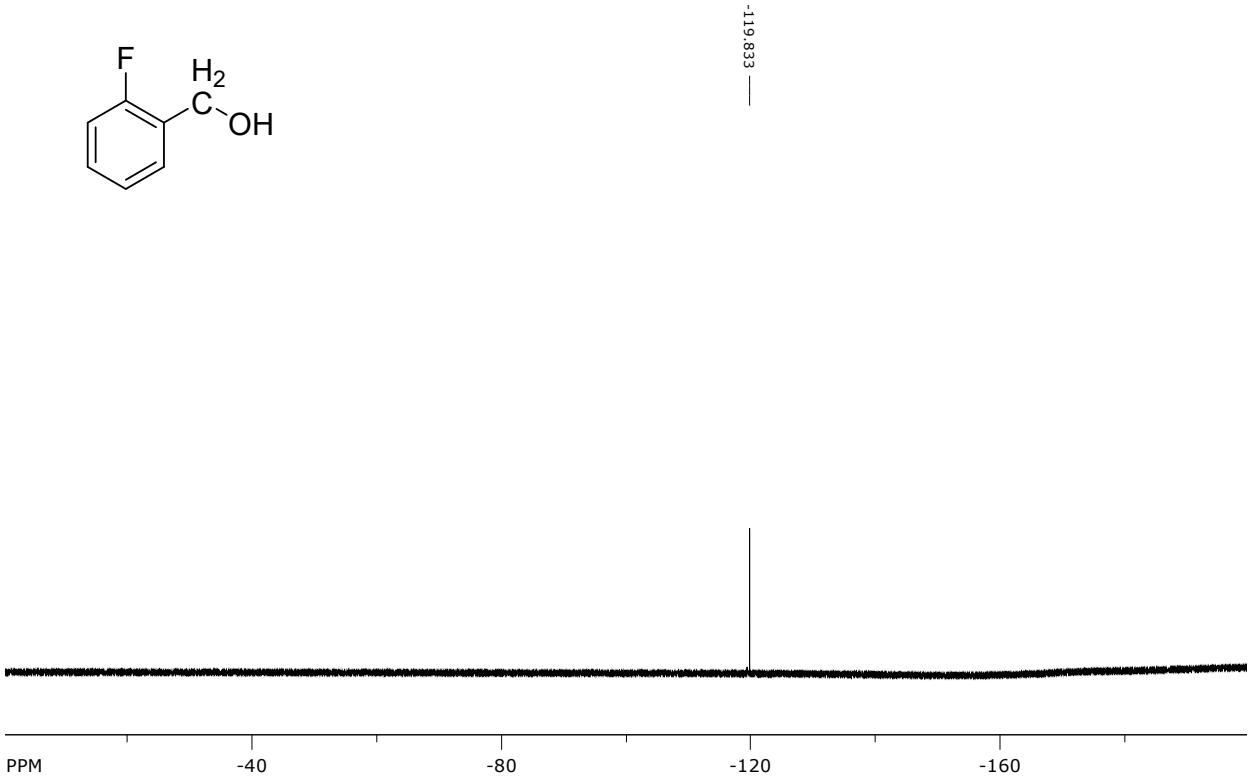

Figure S41. ^{19}F NMR spectrum of 2'-fluorobenzylalcohol ($CDCl_3$, 376 MHz).

S-6. Reaction of 2-BPh_4 with $HSi(OEt)_3$

To a 20 mL Schlenk tube, complex **2-BPh_4** (62.2 mg, 0.058 mmol), $HSi(OEt)_3$ (365 μL, 1.917 mmol) and KO^{t}Bu (33.1 mg, 0.29 mmol) were added and the mixture was dissolved in acetonitrile (2.0 mL) at room temperature in the globe box. Upon addition of acetonitrile, the solution bubbled vigorously. The solution was heated at 50 °C and stirred for 24 h. The resulting mixture was filtered through celite and all the volatiles were removed under reduced pressure. Then, the residual solid was washed several times with n-hexane and dried to obtain dark-green powder (55.7 mg).

(a)

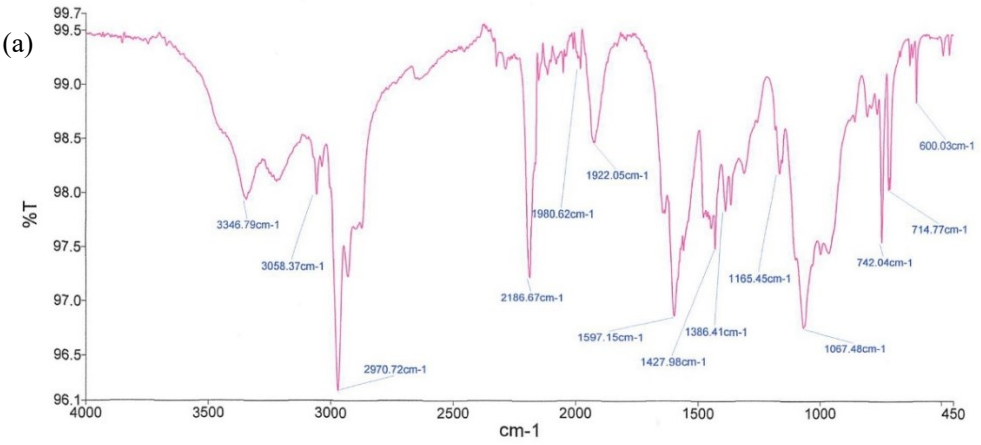

(b)

(c)

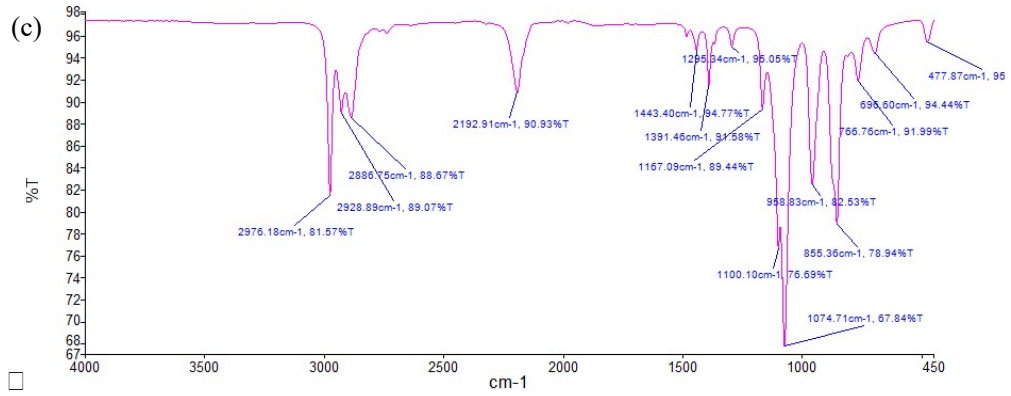

Figure S42. IR spectra of (a) the mixture from the reaction of **2-BPh$_4$** with HSi(OEt)$_3$ and KO^{t}Bu in CH_3CN, (b) complex **2-BPh$_4$** and (c) HSi(OEt)$_3$ (only). Comparing the spectrum (a) from (b), carbonyl absorbances at 2043 and 1992 cm^{-1} disappeared and new bands at 2187 and 1922 cm^{-1} appeared, which were not assigned as HSi(OEt)$_3$ in (c).